JGR Atmospheres

RESEARCH ARTICLE
10.1029/2019JD031996

Influence of Lead width on the Turbulent Flow Over Sea Ice Leads: Modeling and Parametrization

Janosch Michaelis[1], Christof Lüpkes[1], Xu Zhou[2], Micha Gryschka[2], and Vladimir M. Gryanik[1,3]

[1]Alfred Wegener Institute Helmholtz Centre for Polar and Marine Research, Bremerhaven, Germany, [2]Institute for Meteorology and Climatology, University of Hannover, Hannover, Germany, [3]A. M. Obukhov Institute of Atmospheric Physics, Russian Academy of Sciences, Moscow, Russia

Key Points:
- Improved parametrization of inhomogeneous turbulent convection over sea ice leads of variable width for non-eddy-resolving atmospheric model
- Simulated lead effects on atmospheric boundary layer obtained with new nonlocal scheme agree well with large eddy simulation
- Results obtained with local scheme show potential difficulties for mesoscale atmospheric studies in lead-dominated sea ice regions

Supporting Information:
- Supporting Information S1

Correspondence to:
J. Michaelis,
janosch.michaelis@awi.de

Citation:
Michaelis, J., Lüpkes, C., Zhou, X., Gryschka, M., & Gryanik, V. M. (2020). Influence of lead width on the turbulent flow over sea ice leads: modeling and parametrization. *Journal of Geophysical Research: Atmospheres*, *125*, e2019JD031996. https://doi.org/10.1029/2019JD031996

Received 6 NOV 2019
Accepted 3 JUN 2020
Accepted article online 9 JUN 2020

Abstract A new turbulence parametrization is developed for a non-eddy-resolving microscale model to study the effects of leads (elongated open-water channels in sea ice) of different width on the polar atmospheric boundary layer (ABL). Lead-dominated sea ice regions are characterized by large horizontal inhomogeneities of the surface temperature causing strong convection. Therefore, the new parametrization is based on a previous formulation where inhomogeneous conditions of dry convection over leads and nonlocal effects on heat fluxes had already been taken into account for a fixed lead width. A nonlocal lead width dependent approach is applied now for both heat fluxes and momentum fluxes in the convective region. Microscale model results obtained with the new, the previous nonlocal, and a local parametrization are shown, where 10 idealized cases of a lead-perpendicular, near-neutral ABL-flow below a strong capping inversion are considered. Furthermore, time-averaged large eddy simulation (LES) results of those cases are considered for analyzing the integrated effects of the dry convection on ABL characteristics. Microscale model results obtained with the new nonlocal parametrization agree well with the LES for variable lead widths and different atmospheric forcing although there is a room for further improvement. Furthermore, several features obtained with a local closure clearly disagree with LES. Thus, the microscale study also points to difficulties that might occur in mesoscale studies over regions where leads dominate the flow regime when local closures are applied.

1. Introduction

Polar sea ice forms an important component of the Earth's climate system. It reduces the release of heat from the relatively warm ocean into the cold atmosphere, especially between late autumn and spring. However, even in the central polar regions, there are always openings of different shape in the closed sea ice cover, so-called polynyas and leads, mainly due to divergent sea ice drift (e.g., Andreas & Cash, 1999; Smith et al., 1990; Tetzlaff et al., 2015). Leads are open-water channels, which are either ice free or covered by thin, new ice. Their shape is often linear, but they can also be curved. As can be seen from in situ observations and satellite images, both their length and width is extremely variable. The length can range from several hundred meters to several hundred kilometers, and the width varies between several meters and a few kilometers (e.g., Andreas et al., 1979; Lindsay & Rothrock, 1995; Miles & Barry, 1998; Tetzlaff et al., 2015). Mainly during winter, when the differences between the near-surface atmospheric flow and the lead surface can amount up to 40 K, the release of heat from leads is around two orders of magnitude larger than the molecular heat transport through the surrounding sea ice (Badgley, 1966; Maykut, 1978). Thus, with a lead coverage of 1% in a certain region, roughly half of the heat transport from the ocean to the atmosphere must then occur through leads (Thorndike et al., 1975). Furthermore, based on data from the SHEBA campaign (e.g., Overland et al., 2000; Pinto et al., 2003), Overland et al. (2000) found that upward heat fluxes over leads are balanced by downward heat fluxes over sea ice. This was also shown by Lüpkes et al. (2008) and Chechin et al. (2019) using a 1D coupled air-ice box model and prescribing a surface consisting of 95 % sea ice and 5% slightly refrozen leads. They found for sea ice concentrations >95% that changing the concentration by 1% causes a mixed layer atmospheric temperature change of up to 3.5 K. Batrak and Müller (2018) show that an explicit consideration of leads in kilometer-scale atmospheric models can even have an impact on atmospheric conditions several hundred kilometers away from the ice edge in the range of 12 hr weather forecast accuracy (see also Müller et al., 2017).

Focusing more on the local effects of leads, the large temperature difference between the near-surface air and the open water causes strong turbulent convection (convective plumes). An internal boundary layer (IBL) develops, which significantly modifies the structure of the polar atmospheric boundary layer (ABL) depending on the meteorological forcing (wind speed and direction, temperature, and stratification) in the lead environment (Tetzlaff et al., 2015). Furthermore, also the geometry of the leads plays an important role, especially the lead width (L). During the Arctic Ice Dynamics Joint Experiment (AIDJEX, Andreas et al., 1979; Paulson & Smith, 1974), measurements were conducted upwind, and downwind of several Arctic leads of different width, based on which Andreas and Cash (1999) found that the heat transport over small leads ($L < 100$ m) is more efficient than over larger ones.

Based on the AIDJEX data and on data obtained over a polynya in the Canadian Archipelago (see Smith et al., 1983), Alam and Curry (1997) developed a fetch-dependent parametrization of the integral (lead-averaged) sensible heat fluxes from leads, and they found those fluxes to be strongly dependent on L. Also Andreas and Cash (1999) found an L-dependence for heat fluxes over small leads, and they proposed a corresponding parametrization of near-surface heat fluxes. Besides the observations used in Alam and Curry (1997), Andreas and Cash (1999) also used data obtained over a refrozen polynya at drifting station North Pole 23 (see Makshtas & Nikolaev, 1991). Using both parametrizations, for the flux calculation of an observed distribution of leads near 80°N, 108°W in 1996, Marcq and Weiss (2012) found up to 55% larger fluxes than with a parametrization ignoring the L-dependence. The surface flux dependence found in all those studies shows that L is an important parameter for the quantification of lead-generated effects.

Besides the cited observational and modeling studies focusing on surface fluxes over leads, several modeling studies of the whole turbulent ABL over leads have been performed, for example using Large Eddy Simulation (LES) models (e.g., Esau, 2007; Glendening & Burk, 1992; Glendening, 1994; Weinbrecht & Raasch, 2001). With LES, large turbulent eddies can be resolved which gives detailed information on the turbulence structure. Glendening and Burk (1992) simulated the lead-perpendicular ABL flow over a 200 m wide lead with a temperature difference of 27 K between water and sea ice surface. Upstream of the lead they prescribed stable stratification and weak wind ($< 2.5\ \mathrm{ms}^{-1}$). They proposed an L-dependent equation for the plume penetration height z_p with $z_p \propto L^{2/3}$. Zulauf and Krueger (2003) transferred that equation to other lead widths and they found rather $z_p \propto L^{1/2}$. Overall, results of both studies show the importance of L also for the quantitative analysis of the convective IBL over leads.

Extensions of the study of Glendening and Burk (1992) were performed by Glendening (1994) regarding the inflow direction and by Weinbrecht and Raasch (2001), who found that the model resolution strongly influences the results, especially in high wind regimes. Esau (2007) investigated leads with different widths for zero geostrophic wind.

Besides pure LES applications, several modeling studies on lead effects using microscale and mesoscale atmosphere models have been carried out (as, e.g., by Alam & Curry, 1995; Dare & Atkinson, 2000; Mauritsen et al., 2005; Lüpkes, Gryanik, et al., 2008, henceforth abbreviated by L08; Li et al., 2020; Wenta & Herman, 2018). Such types of numerical models are used to determine the integral lead effect on the ABL flow, but the structure of single turbulent eddies is not resolved as with LES. Due to grid sizes of usually 10^2 m horizontally and 10^1 m vertically, parametrizations of the turbulent processes are required to close the system of the governing equations. Alam and Curry (1995), Dare and Atkinson (2000), Mauritsen et al. (2005), Wenta and Herman (2018), and Li et al. (2020) use local closures (1.5-, 2-, or 2.5-order turbulent kinetic energy (TKE) schemes, or a first-order Smagorinsky scheme), where the turbulent fluxes are related to the gradients of mean quantities using K-theory (see Stull, 1988). However, especially in the upper half of a homogeneously surface-heated convective ABL, upward heat fluxes are present in regions with neutral or even slightly positive vertical potential temperature gradient (Holtslag & Moeng, 1991). L08 show based on LES results that this holds also for the convective ABL over leads for a near-perpendicular flow in typical springtime conditions. Indications for the existence of these nongradient or counter-gradient fluxes were also found in the aircraft-based measurement study STABLE over the marginal ice zone North of Svalbard in 2013 by Tetzlaff et al. (2015). To account for such phenomena, L08 derived a parametrization for the turbulent sensible heat flux over leads using K-theory, but with a gradient correction scheme based on the parametrization of Lüpkes and Schlünzen (1996), which was derived for horizontally homogeneous conditions. L08 account for the horizontal inhomogeneities over leads by considering the distance to the

lead's upstream edge in their approach and by distinguishing different convective regimes in the plume's core and at its boundaries. They investigated 10 idealized scenarios with $L = 1$ km, an ABL height of 300 m, and different meteorological forcing in a microscale modeling study, where the results obtained with their nonlocal parametrization agreed well with time-averaged LES results.

L08 concluded that their findings could be the basis for studies investigating the impact of lead ensembles in much larger domains by saving computational time with respect to a comparable study using LES. However, they stress that especially L should be taken into account for further improvements of their parametrization. Moreover, since climate models consider rather a fractional sea ice cover than a clear differentiation between open-water and ice surfaces, a detailed investigation on the effects of lead width on the polar ABL seems necessary. This might also help to develop an improved surface flux parametrization over leads for those models, which seems necessary to improve model results not only for the polar regions but also for midlatitudes (Vihma et al., 2014).

Therefore, in this paper, we present a modified version of the parametrization of L08, which includes the lead width as a parameter to be used in small-scale atmosphere models. Results will be compared with new time-averaged LES for 10 different scenarios of a lead-perpendicular flow in the ABL differing by L, wind, and temperature, and we will use those LES results to determine the unknown parameters of the modified closure (henceforth called new closure or new parametrization). Thus, the main goal of our study is to derive, based on LES, an improved parametrization of turbulent fluxes over leads in compact sea ice for non-eddy-resolving microscale models. We also aim to investigate drawbacks related to local closures applied on this scale.

The new parametrization is designed for idealized conditions. It represents another step towards turbulence closures designed for small-scale atmospheric models for convective processes in strongly inhomogeneous conditions, after the first step was made by L08. However, further development is necessary in the future, for example, to include moisture transport. We also show that the reproduction of detailed flow structures related to leads requires, independent on the used closure, horizontal grid sizes not larger than $L/5$ to obtain a reasonable agreement with LES.

2. Models

As L08, we use two different atmospheric model types, an LES model and a non-eddy-resolving small-scale model. For the non-eddy-resolving model, a parametrization of the subgrid scale turbulence is required to quantify the integral effects of the turbulent eddies. The LES model allows a much more detailed analysis of the turbulent flow over leads since the individual eddies on all relevant turbulent scales are resolved. With both models, scenarios of a lead-perpendicular flow in the ABL are simulated, where the upstream ABL is capped by a strong inversion of height $z_i = 300$ m. A sketch of such a flow regime over a lead of width L is shown in Figure 1.

2.1. LES Model

For LES, we use the PArallelized Large Eddy Simulation Model PALM (Maronga et al., 2015; Raasch & Schröter, 2001) with revision number 2864 in its dry version. PALM has already been used to study polar boundary layers over heterogeneous sea ice distributions (Weinbrecht & Raasch, 2001), small-scale processes above leads (L08), and large-scale processes concerning the impact of sea ice heterogeneities on the downstream ABL in cold air outbreaks (de Roode et al., 2019; Gryschka et al., 2008, 2014). PALM is based on the nonhydrostatic Boussinesq-approximated Reynolds equations with a 1.5-order subgrid scale closure according to Deardorff and Peterson (1980), in which a prognostic equation of the subgrid scale TKE is solved. The Poisson equation for pressure is solved with the multigrid method and for the advection terms the fifth-order Wicker-Skamarock scheme is used. For time integration, the third-order Runge-Kutta scheme is applied.

At the lead-perpendicular lateral boundaries, cyclic boundary conditions are applied. At the lead-parallel inflow boundary, fixed vertical profiles of wind and temperature are prescribed. At the corresponding outflow, a zero gradient is prescribed for temperature, while for the wind components a radiation boundary condition is set. The latter condition assumes that wind components are advected with a transport velocity, which includes wave propagation and advection by the wind itself (see Orlanski, 1976).

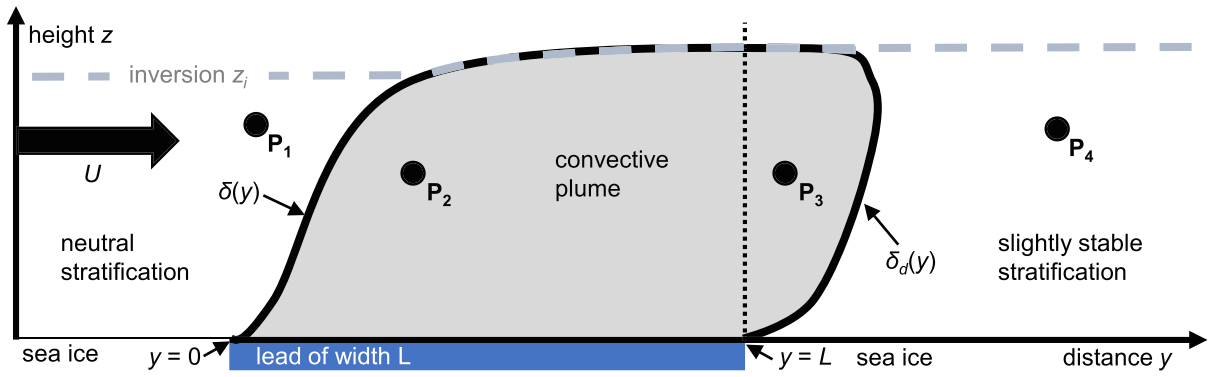

Figure 1. Sketch of a convective plume developing in an ABL of height z_i over a polar lead of width L during a lead-perpendicular flow (here: from left to right). Stratification of the incoming flow, where U is the vertically averaged horizontal wind speed, is neutral, and the lead causes stabilization of the ABL in the downstream region. The convective plume area is defined as the region between the upper and lower boundaries of the internal boundary layer (IBL), $\delta(y)$ and $\delta_d(y)$, where y is the distance to the lead's upstream edge. P_1 to P_4 represent arbitrary points in different regimes of the ABL-flow: P_1 is upstream of the convective plume, P_2 and P_3 are inside the plume at $0 \leq y \leq L$ and $y>L$, respectively, and P_4 is downstream of the plume. The dotted vertical black line marks the downstream lead edge. Modified after L08 and Tetzlaff et al. (2015).

To guarantee that resolved turbulent structures reach the upstream edge of the lead, a so-called turbulence recycling method after Lund et al. (1998) and Kataoka and Mizuno (2002) was applied. In a certain distance downstream of the inflow (here: 5 km), deviations of the velocity components from their lateral mean are taken as turbulent signals and superimposed on the inflow profiles at each time step. This method was not applied in L08. For more details on the implementation of the boundary conditions and turbulence recycling method, see Maronga et al. (2015).

Compared to the LES in L08, we chose a smaller grid spacing of 5 m (instead of 10 m) in all directions due to increased computational capacity in the last years. Therefore, in contrast to L08, also the shallow convection in the first half of the leads is resolved. To prove this, we compared xz-cross sections of the resolved and subgrid scale TKE as well as of the resolved and subgrid scale heat flux (not shown). Furthermore, for case L5c-U5 (see Table 1 in section 2.3), we tested the reliability of the model resolution by performing additional simulations with 10 and 2.5 m grid spacing, where we found that results do not differ significantly between 5 and 2.5 m grid spacing (not shown). The vertical grid spacing is equidistant up to $z = 300$ m and smoothly stretched above. The model's top is at $z = 3014$ m. In lead-parallel direction, the model domain of PALM has an extension of 640 m, so more than $2z_i$, to capture also the larger convective structures that contribute to the turbulent fluxes.

Since with the applied spatial resolution the detailed structure of the turbulent eddies is simulated, wind and temperature are strongly variable both spatially and temporally. Therefore, to ensure comparability with the results from the non-eddy-resolving model in its 2-D version, LES results are averaged in lead-parallel direction and time (see Zhou & Gryschka, 2019, for the data).

2.2. Microscale Model

2.2.1. Model Description

We follow the methods of L08 and use the nonhydrostatic atmospheric model METRAS (MEsoscale Transport and Stream Model; Schlünzen, Bungert, et al., 2012; Schlünzen, Flagg, et al., 2012) in a dry and 2-D version for microscale simulations of lead scenarios. The Boussinesq-approximated model equations are solved on a staggered ARAKAWA-C grid and for all considered cases with $L \geq 1$ km grid spacing is similar to L08 (200 m horizontally and at least 20 m in vertical direction). For another scenario with $L = 500$ m, the horizontal grid spacing is 100 m. A sensitivity study regarding the horizontal grid spacing shows that the grid size should not be larger than $L/5$ for an appropriate resolution of the lead-generated convection (see Appendix C1). Moreover, we aim to avoid an overlap of resolved and subgrid scale transport as far as possible. Thus, we assume that the turbulent transport in METRAS is completely due to subgrid scale processes in the convective region, which is why we did not consider horizontal grid sizes < 100 m. We also tested model simulations with 10 m vertical grid spacing, but results of those simulations were disturbed by resolved but unrealistic gravity waves (not shown). Unlike L08, we use an equidistant vertical grid

spacing for the entire ABL which results in 15 instead of 10 layers below $z = 300$ m. Above $z = 300$ m, the model consists of another 50 layers, and the model's top is at about 9,600 m ensuring that gravity waves are damped towards the model's top. Following the strategy of L08, we also do not consider radiation explicitly or condensation processes.

As in the LES model, we prescribe fixed values for temperature at the inflow boundary. For the outflow boundary, we apply a zero gradient condition. For the wind components, boundary conditions are the same at inflow and outflow boundary. Boundary-parallel wind components are calculated from zero gradient boundary condition and boundary-normal wind components are calculated directly as far as possible (see Schlünzen, Bungert, et al., 2012; Schlünzen, Flagg, et al., 2012).

2.2.2. Local and Nonlocal Turbulence Parametrizations in METRAS

Since we focus on simulations of a dry atmosphere, we will use the term heat flux for sensible heat fluxes, unless stated otherwise. For the parametrization of both heat and momentum fluxes, local and nonlocal approaches are considered.

2.2.2.1. Local Mixing-length Closure:

The local closure schemes are based on flux-gradient relationships

$$\overline{w'\theta'} = -K_h \frac{\partial \overline{\theta}}{\partial z}, \tag{1}$$

for temperature, where $\partial\overline{\theta}/\partial z$ is the vertical potential temperature gradient and K_h is the eddy diffusivity for heat, and

$$\overline{w'u'} = -K_m \frac{\partial \overline{u}}{\partial z}, \qquad \overline{w'v'} = -K_m \frac{\partial \overline{v}}{\partial z}, \tag{2}$$

for momentum, where $\partial\overline{u}/\partial z$ and $\partial\overline{v}/\partial z$ are the vertical gradients of the x- and y-components of the wind vector and K_m is the eddy diffusivity for momentum. In the surface layer (first grid cell above the surface) both K_m and K_h are calculated according to Monin-Obukhov similarity theory using Businger-Dyer functions (Businger et al., 1971; Dyer, 1974). Above the surface layer, a mixing-length approach by Herbert and Kramm (1985) is applied to calculate K_m and K_h in Equations 1 and 2:

$$K_m = \begin{cases} l_n^2 \left|\frac{\partial \mathbf{v_h}}{\partial z}\right| (1 - 5Ri)^2 & \text{for } 0 \le Ri \le Ri_c \\ l_n^2 \left|\frac{\partial \mathbf{v_h}}{\partial z}\right| (1 - 16Ri)^{1/2} & \text{for } Ri \le 0 \end{cases} \tag{3}$$

$$K_h = \begin{cases} K_m & \text{for } 0 \le Ri \le Ri_c \\ K_m (1 - 16Ri)^{1/4} & \text{for } Ri \le 0 \end{cases}, \tag{4}$$

where Ri is the Richardson number, Ri_c is the critical Richardson number, for which 0.199 is used instead of 0.2 to avoid zero diffusion, $\partial\mathbf{v_h}/\partial z$ is the vertical gradient of the horizontal wind, and $l_n = \kappa z/(1+\kappa z/l_{max})$ is the mixing length for neutral stratification with Kármán's constant κ. For the determination of l_n, as in L08, we set the maximum mixing length $l_{max} = 0.15 z_i$. Originally, this relation was derived by Brown (1996) based on LES. At grid points where $Ri > Ri_c$, both K_m and K_h are calculated with $Ri = Ri_c$. This choice guarantees matching with the surface layer when Businger-Dyer functions are used in case of stable stratification.

Equations 3 and 4 guarantee continuity of the fluxes at the first grid level. Note that, for example, Grachev et al. (2013) found that a critical Richardson number probably does not exist in nature, and an alternative closure is proposed for stable stratification. However, here we do not consider the related implications since in the surface layer the stratification is far from the critical value in all model simulations (not shown).

2.2.2.2. Nonlocal Closure of L08

Based on their LES results, L08 found that counter-gradient heat fluxes occur in the convective plume region (Figure 1). Those fluxes do not depend on local gradients and have to be parametrized with nonlocal parameters. Thus, L08 formulated their parametrization based on

$$\overline{w'\theta'} = -K_h\left(\frac{\partial\overline{\theta}}{\partial z} - \Gamma\right), \tag{5}$$

with the counter-gradient correction Γ. Equation 5 was first proposed by Priestley and Swinbank (1947) and theoretically derived by Deardorff (1972) and Holtslag and Moeng (1991). The latter formulated Equation 5 for horizontally homogeneous conditions, where K_h and Γ are given as functions of z/z_i, with the ABL height z_i, the convective velocity scale w_* (also called Deardorff's convective velocity scale, e.g., Deardorff, 1970), and the convective temperature scale θ_f. The latter two quantities are written as follows:

$$w_* = (B_s z_i)^{1/3}, \tag{6}$$

with the surface buoyancy flux B_s, where

$$B_s = \frac{g}{\theta_0}\overline{w'\theta'}|_s, \tag{7}$$

where g is the gravitational acceleration, θ_0 is the surface layer temperature, and $\overline{w'\theta'}|_s$ is the kinematic surface heat flux, and

$$\theta_f = \frac{\overline{w'\theta'}|_s}{w_*}. \tag{8}$$

Following Holtslag and Moeng (1991), Lüpkes and Schlünzen (1996) derived K_h and Γ in a way which ensures continuous fluxes at the top of the surface layer. In those equations, w_* acts as scaling velocity, which is defined in Equation 6 for convection over a horizontally homogeneous surface and a horizontally homogeneous ABL height z_i. To account for the nonhomogeneous flow regime over leads, L08 adjusted the nonlocal closure of Lüpkes and Schlünzen (1996). We will briefly describe their principles and use Figure 1 to illustrate the respective steps.

L08 assume that heat transport inside the convective plume (e.g., at P_2 and P_3) is dominated by nonlocal effects while outside (e.g., at P_1 and P_4) mixing is local. As switching lines between the two closures they consider the upper and the lower plume boundaries $\delta(y)$ and $\delta_d(y)$ (also called upper and lower IBL height), where y is the distance to the lead's upstream edge. Furthermore, the functional relations of K_h and Γ remain the same as over a homogeneous surface, but z_i is replaced by the fetch-dependent IBL height $\delta(y)$. Moreover, L08 state that the heat flux at any position inside the convective plume is determined by the lead-averaged surface buoyancy flux B_l (same as B_s, but with the index l for the lead's surface). Thus, also at P_3, which is downstream of the lead but still inside the plume, the characteristics are dominated by the convection generated over the lead. Besides B_l, the dominating parameters inside the plume are the vertically averaged horizontal wind speed in the ABL at the lead's upstream edge (U) and the upstream ABL height z_i. Moreover, z_i is set constant because L08 consider only cases with neutral stratification in a shallow ABL capped by a strong inversion.

To match the nonlocal and local closures, L08 propose a new formulation of the convective velocity scale (called w_l to avoid confusion). They assume that for the region above the lead ($0 < y < L$, Figure 1) w_l can be expressed by $(B_l\delta(y))^{1/3}$, which is similar to Equation 6, but with $\delta(y)$ instead of z_i. However, to take into account lateral entrainment and dissipation for $y > L$, which cause decaying convection, an exponential decay of w_l is assumed. Moreover, L08 focused on narrow leads ($L \approx 1$ km) where the horizontal extension of the plume into the lead's downstream region can exceed L by several kilometers ($L \ll D$, where D is a decay length scale specified below). Thus, they neglected L as a governing parameter and applied their decay function already at $y = 0$:

$$w_l(y) = c(B_l\delta(y))^{1/3}\exp(-y/D), \tag{9}$$

with c as an adjustable parameter and with D gained from an equation for $\delta(y)$. The latter is derived by integrating

$$\frac{d\delta}{dy} = \frac{w_e(y)}{U} = \frac{a_e w_{max}(y)}{U} = \frac{a_e a_m w_l(y)}{U}, \tag{10}$$

which follows Monin and Yaglom (1971) and Turner (1986), where w_e is the entrainment velocity, w_{max} is the velocity of the strongest eddies, and a_e and a_m are parameters connecting w_e, w_{max}, and w_l. By integrating Equation 10, L08 obtained

$$\delta(y) = \delta_{max}\left(1 - \exp\left(-y/D\right)\right)^{3/2} = z_i\left(1 - \exp\left(-y/D\right)\right)^{3/2}, \tag{11}$$

where $\delta_{max} = z_i$ is the maximum upper IBL height for a neutral environment, wherein convective turbulence always penetrates up to the inversion. Since

$$\delta_{max} = \left(\frac{2a}{3}\frac{B_l^{1/3}D}{U}\right)^{3/2}, \tag{12}$$

with $a = a_e a_m c$, D can be written as

$$D = \frac{3}{2a}\left(\frac{U^3}{B_l}\right)^{1/3} z_i^{2/3}. \tag{13}$$

For the determination of $\delta_d(y)$, L08 assume that this switching line is located downstream of the lead where the nonlocal heat flux is less than $F_{crit} = 2\,\mathrm{Wm}^{-2}$. For the parameters, L08 define the following ranges: $c \approx 1.6 \pm 0.5$, $a_m = 3 \pm 1$, and $a_e = 0.3 \pm 0.1$ so that a is in a range between 0.4 and 3.4. For all their cases, L08 applied $a = 2.3$ and $c = 1.6$. For the convective temperature scale θ_f in the plume, which we call θ_l to avoid confusion with the usual definition, L08 consider Equation 8 with $w_l(y)$ instead of w_*. Momentum fluxes are parametrized with the local closure (Equations 2 and 3).

L08 reformulated the equations of Lüpkes and Schlünzen (1996) for K_h and Γ in a nondimensional form as a function of the stability parameter

$$S(y) = w_l(y)/u_* \tag{14}$$

and of the nondimensional vertical coordinate

$$Z(y) = z/\delta(y) \tag{15}$$

and obtained

$$K_h/K_p = Z\left(1 + \frac{S}{\kappa}Z^{1/3}\right)(1 - Z)^2,\ Z_p \le Z \le 1, \tag{16}$$

with the eddy diffusivity at the surface layer's top z_p

$$K_p = \frac{u_*\kappa z_p}{\Phi_p}, \tag{17}$$

where $\Phi_p = (\Phi_h|_{z_p} + \Phi_\Gamma)Z_p(1 + (S/\kappa)Z_p^{1/3})(1 - Z_p)^2$ with the Monin-Obukhov similarity function for heat Φ_h and with $\Phi_\Gamma = \Gamma|_{z_p}\kappa z_p u_*/\overline{w'\theta'}|_s$.

For Γ, L08 obtained:

$$\Gamma/\Gamma_0 = 0.63bS\left[(1 - Z)^{3/2} + 0.593S^3 Z(1 - 0.9Z)^{3/2}\right]^{-2/3}, \tag{18}$$

with an adjustable parameter b and with $\Gamma_0 = (\overline{w'\theta'}|_s)/(u_*\delta(y)) = S\theta_l/\delta(y)$. L08 set $b = 0.6$, which is much lower as in previous studies (e.g., Holtslag & Moeng, 1991; Lüpkes & Schlünzen, 1996).

Table 1
Summary of Discussed Cases

Wide leads	L5c-U3	L5c-U5	L5c-U7	L10c-U5	L5w-U5
L (km)	5	5	5	10	5
u_g (ms^{-1})	3.0	5.0	7.0	5.0	5.0
v_g (ms^{-1})	0.4	1.0	2.0	1.0	1.0
T_{ice} (K)	250	250	250	250	260
$\overline{F_s}$ (Wm^{-2})	144	195	245	196	85
$F_{100,L}$ (Wm^{-2})	119	163	197	169	75
$F_{100,M}$ (Wm^{-2})	127	168	205	169	68
$F_{200,L}$ (Wm^{-2})	74	102	113	103	49
$F_{200,M}$ (Wm^{-2})	73	95	115	94	39
Narrow leads	**L1c-U3**	**L1c-U5**	**L1c-U7**	**L1w-U10**	**L0.5c-U5**
L (km)	1	1	1	1	0.5
u_g (ms^{-1})	3.0	5.0	7.0	10.0	5.0
v_g (ms^{-1})	0.4	1.0	2.0	2.5	1.0
T_{ice} (K)	250	250	250	260	250
$\overline{F_s}$ (Wm^{-2})	125	163	200	131	166
$F_{100,L}$ (Wm^{-2})	83	103	117	21	51
$F_{100,M}$ (Wm^{-2})	103	96	91	27	48
$F_{200,L}$ (Wm^{-2})	34	41	41	4	15
$F_{200,M}$ (Wm^{-2})	60	43	40	11	21

Note. L is the lead width, u_g and v_g are the lead-orthogonal and lead-parallel geostrophic wind components, T_{ice} is the prescribed sea ice surface temperature, $\overline{F_s}$ is the lead-averaged surface heat flux, $F_{100,L}$ and $F_{200,L}$ are the maximum heat fluxes at 100 m and 200 m height as simulated with LES, and $F_{100,M}$ and $F_{200,M}$ are the corresponding values as simulated by the microscale model using the new nonlocal turbulence parametrization (section 5.1). For the cases with $L =$ 1 km, results correspond to the second lead 10 km downstream of another lead.

2.3. Scenarios and Setup of Models

We discuss the results of 10 different idealized scenarios (Table 1). Nevertheless, our applied model domains are chosen with respect to observations during several campaigns (REFLEX I and II, ARTIST, ARKXIX/1, STABLE, Hartmann et al., 1992, 1999; Kottmeier et al., 1994; Lüpkes et al., 2004; Tetzlaff et al., 2015) and the initialization data for the simulations are representative for typical springtime conditions in the polar regions.

We distinguish between the convection over wide and over narrow leads. We define wide leads as those where the convection penetrates into the capping inversion already above the leads. Here, this concerns four scenarios with $L = 5$ km and one with $L = 10$ km. For narrow leads, where the convection reaches the inversion further downstream, we consider four scenarios with $L = 1$ km similar to those in L08 and one scenario with $L = 0.5$ km. We focus on results over one lead, but for the cases L1c-U3, L1c-U5, L1c-U7, and L1w-U10 (Table 1) as in L08, we consider the results over a lead 10 km downwind of another lead to compare them with the L08 results. This ensures that the effects caused by the first lead, such as slightly increased air temperature and a slightly stable stratification upstream of the second lead, are included.

As L08, we focus on cases with sea ice surface temperatures prescribed to 250 or 260 K. Surface temperature of the leads is always prescribed to 270 K representing a lead covered by thin, new ice, which is often observed at low air temperatures (Pinto et al., 2003). For both surfaces, temperatures do not change throughout the model integration.

Four different wind regimes are investigated prescribing lead-orthogonal geostrophic wind components u_g upstream of the leads of 3, 5, 7, and 10 ms^{-1}, respectively. The corresponding lead-parallel components, v_g, (see Table 1) ensure a lead-perpendicular flow in the ABL. Thus, all simulations can be regarded as quasi-2-D simulations, independent of the lead-parallel component of the coordinate system. That is, we neglect a possible fetch dependence of surface roughness and prescribe the roughness lengths for momentum to $z_0 = 10^{-3}$ m over ice and $z_0 = 10^{-4}$ m over water in both models. For both surfaces, the ratio between the roughness lengths for momentum and heat is assumed as 10. The value of the Coriolis parameter refers to 79°N.

As in L08, a neutrally stratified atmosphere with a strong capping inversion at $z_i = 300$ m is prescribed initially in the whole domain of both models and as inflow temperature profile during the whole time integration. The initial and inflow profile of wind in METRAS is determined with the 1-D model version. In PALM, a 3-D LES prerun with lateral cyclic boundary conditions and smaller model domain than in the main run representative for the situation over ice was performed. Thus, unlike L08, we use a 3-D instead of a 1-D prerun to initialize the simulations with a turbulent wind field. Hence, at the inflow boundary, the turbulence is produced already at the beginning of each simulation due to the turbulence recycling method causing a faster developing flow.

For both models, we prescribe at least 5 km distance for both inflow and outflow boundary to the corresponding lead edges to guarantee that results near the lead are not influenced by the boundaries. In two-lead domains, we prescribe a gap of at least 10 km to the next lead to avoid possible interactions of plumes from different leads.

The model simulations are performed until quasi-stationary conditions are reached with respect to temperature, wind, and flux profiles in the ABL. For METRAS, quasistationarity is reached after approximately 2 hr integration time. With PALM also approximately 2 hr are required to reach quasistationarity, but the total simulation time is longer since the LES results are then averaged over an hour.

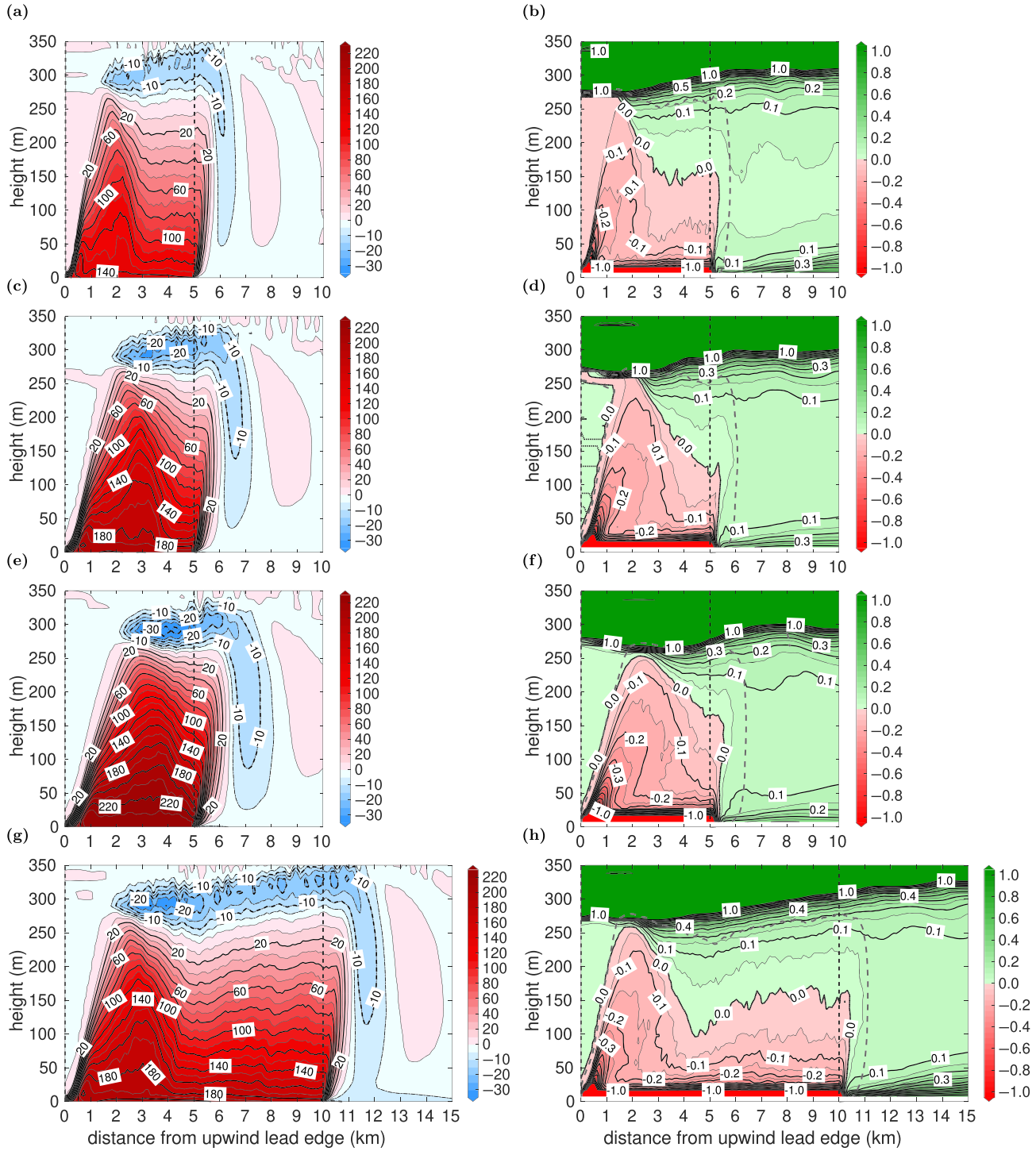

Figure 2. LES results of sensible heat flux in Wm^{-2} (left column) and of vertical potential temperature gradient in K per 100 m (right column) for the cases L5c-U3 (a, b), L5c-U5 (c, d), L5c-U7 (e, f), and L10c-U5 (g, h). The position of the lead is between 0 km and the vertical dashed black line. The distance between heat flux contour lines is 5 Wm^{-2} for negative fluxes. In the right column, the area inside the dashed gray lines depicts the region of positive fluxes inside the convective plume.

3. LES Results

Time-averaged LES results are presented for the heat flux, vertical potential temperature gradient (Figure 2), horizontal wind speed, and momentum flux (Figure 3). Both figures show results of the cases L5c-U3,

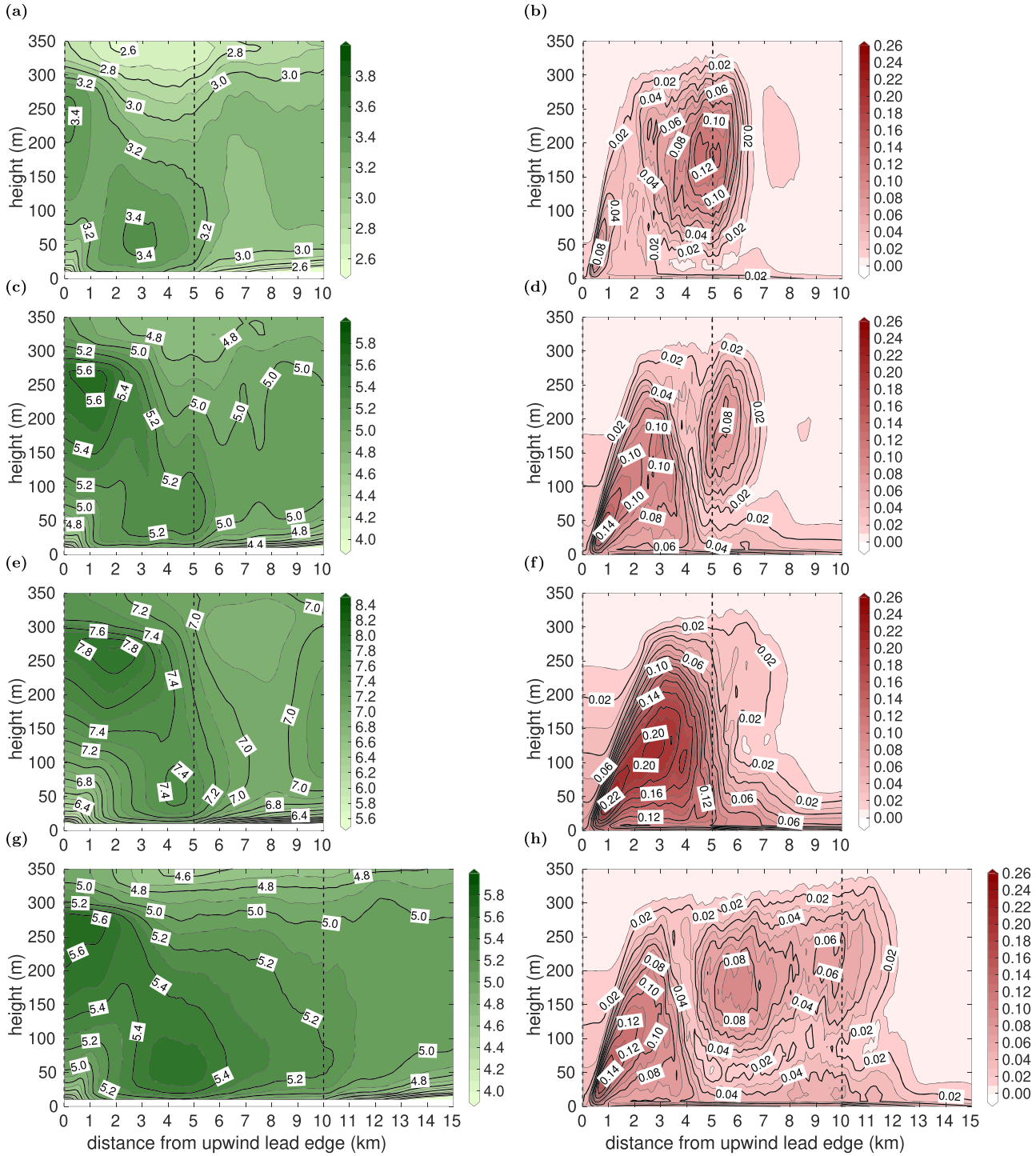

Figure 3. LES results as in Figure 2, but horizontal wind speed in ms^{-1} (left column) and vertical momentum flux in Nm^{-2} (right column) are shown.

L5c-U5, L5c-U7, and L10c-U5 (Table 1). Thus, in three cases, the same lead width of 5 km and the same inflow temperature but different wind speeds are used. In case L10c-U5, the lead width L is doubled. The position of the lead in each plot is between $y = 0$ km and the dashed vertical black line, where y is the distance from the upstream lead edge. The flow is from left to right. For the heat flux, the sum of both resolved and subgrid scale fluxes is shown in Figure 2 (left column). Values of the vertical potential temperature gradient are shown in Figure 2 (right column) in K per 100 m.

In three cases, the overall structure of the heat flux patterns seems to be similar (Figures 2a, 2c, and 2e). Above the lead, positive heat fluxes are simulated almost in the entire ABL. At that distance where the convective plume reaches the capping inversion, entrainment is generated with negative fluxes due to turbulence in the inversion layer. The horizontal distribution of heat fluxes is highly inhomogeneous showing a clear maximum over the lead. In the upper third of the mixed layer, the position of this maximum occurs where the plume starts to penetrate into the inversion. Towards the lower part of the mixed layer, the position is shifted slightly downstream. Especially for case L5c-U3, a region of almost horizontally homogeneous heat fluxes is simulated downwind of the maximum, starting at approximately $y = 3$ km (Figure 2a). For all three cases, the plume extends also into the downwind region of the lead, followed by a region of negative (downward) fluxes in the entire ABL.

Figures 2a, 2c, and 2e clearly demonstrate the influence of the upstream wind speed on the spatial structure and strength of the lead-generated convection. The higher the wind speed, the higher is the inclination angle of the plume, the stronger is the entrainment, and the stronger is the lead-averaged surface heat flux (see also Table 1). Furthermore, with increasing wind speed, the distances of the simulated maximum heat fluxes from the upstream lead edge increase. However, the maximum is more pronounced for weak wind (Figure 2a) than for strong wind (Figure 2e). The simulated heat flux distribution over the lead with $L = 10$ km (Figure 2g) looks similar to the corresponding case with $L = 5$ km (Figure 2c) until $y \approx 6$ km. Also in the 10 km-case, a maximum is simulated at $2.5 < y < 3$ km and the entrainment fluxes in the inversion layer reach similar values. Furthermore, the positions of the maximum entrainment fluxes with fetch denote an almost linear growth in ABL thickness for $4\,\text{km} < y < L$. Such an increase is also shown for case L5c-U5, but less strong (Figure 2c). Obviously, an increase in lead width leads to a stronger increase in ABL thickness over the lead, which has been studied also for other cases (not shown).

The vertical potential temperature gradient (Figure 2, right column) indicates the ABL stratification near the lead. An almost neutrally stratified ABL up to $z \approx 270$ m at the lead's upstream edge is obtained in all cases. This means that the bottom of the inversion is lower at the lead's upstream edge after some simulation time than its initial position at $z = 300$ m at the inflow boundary. This subsidence is probably caused by a thermally induced convergence directly below the inversion near the lead's upstream edge. Moreover, it is also shown in the corresponding microscale model results (sections 4 and 5.2). Strong unstable stratification occurs above the lead surface and a stabilization is seen downwind over sea ice.

Comparing the vertical potential temperature gradient in the convective area with the region of positive heat fluxes (dashed gray lines in Figure 2, right column), there is a clear evidence for nongradient heat fluxes. These fluxes roughly start at that distance where the plume reaches the inversion and they dominate the heat flux pattern especially in the upper part of the ABL near $y = L$ and further downwind. The higher the wind speed, the further those counter-gradient fluxes extend into the downstream region. These results for heat fluxes and stratification agree well with those discussed by L08.

The general structure of the wind field (Figure 3, left column) seems to be independent on the inflow wind speed. For example, in all cases, pronounced wind speed maxima are simulated at the lead's upstream edge with maximum values directly below the inversion. Although these maxima exceed the mean wind speed by only about 10%, we will call them in the following low-level jet (LLJ). Due to lead-generated convection and, thus, enhanced vertical mixing, the LLJ near the inversion is destroyed and another, slightly less pronounced wind maximum is simulated between approximately $30 < z < 100$ m. The higher the upstream wind speed, the larger are the distances of both maxima from the lead's upstream edge due to increased plume inclination. In the lead's downstream region not directly influenced by the convection, there is some evidence for a recovering LLJ.

Unlike L08, we also analyze vertical momentum fluxes, for which LES results are shown in Figure 3 (right column). As for the previously discussed quantities, also the structure of the simulated momentum flux distributions is, basically, similar in all cases, and strong horizontal inhomogeneity is obvious. Moreover, two pronounced maxima are shown. The first maximum is simulated in the unstable region over the lead close to the lead's upstream edge and its magnitude at $0.1z_i$ increases with increasing wind speed. Another, slightly less pronounced maximum is simulated near the lead's downstream edge. This secondary maximum is especially pronounced in the cases L5c-U3 and L10c-U5 (Figures 3b and 3h), and its center is near $0.6z_i$. For those two cases, heat fluxes are almost horizontally homogeneous in that part of the ABL (Figures 2a and 2g). The

secondary maximum in the momentum fluxes is not simulated for the case L5c-U7 (Figure 3f). In this case, the region of horizontally inhomogeneous heat fluxes extends into the lead's downwind region (Figure 2e). In contrast to the first maximum of the momentum flux patterns, the magnitude of the secondary maximum decreases with increasing upstream wind speed.

4. Microscale Model Results with Different Turbulence Closures

In this section, we consider results for case L5c-U5 obtained with METRAS for the same quantities as in section 3 using the turbulence closures described in section 2.2.2. Results in Figure 4 (left column) were obtained with the local closure, those in Figure 4 (right column) with the L08 closure.

As already stated by L08 and as mentioned in the previous sections, nongradient heat fluxes occur in the convective environment over leads. Thus, it is not surprising that both heat fluxes and stratification obtained with METRAS using the local closure (Figures 4a and 4c) disagree with the corresponding LES results (Figures 2c and 2d). Especially, the stratification downstream of the lead is not represented correctly. No entrainment is simulated, and positive heat fluxes occur over a wide region of several kilometers width downstream of the lead. Also, the positions of maximum heat fluxes disagree with the corresponding LES results.

The lead-generated effects on the wind field (Figure 4e) are partly represented with the local closure. The maximum value and the position of the LLJ upstream of the lead agree well with the corresponding LES results (Figure 3c) and also a destruction of the LLJ over the lead is simulated. However, this destruction is not as effective as compared to LES.

In the momentum flux distribution obtained with the local closure (Figure 4g), the position of the main maximum near the upstream edge of the lead agrees with LES (Figure 3d), but it is not as pronounced as in LES. Another maximum is simulated near $y = L$, but it occurs at $z \approx z_i$ rather than at $z \approx 0.6z_i$ as in the LES result. Moreover, this maximum seems to be caused by processes that are not simulated with LES, namely, by an unstable stratification at that location in combination with high vertical wind shear $\partial \mathbf{v_h}/\partial z$ near $z = z_i$ (see also Figure S1 in the supporting information).

Not only an improvement but also a drawback is obvious when the L08 closure is used (Figure 4b). A pronounced maximum of heat fluxes is simulated at $y \approx 2$ km, but a strong discontinuity occurs at $y \approx 4.5$ km near the downstream lead edge. We found this discontinuity is sensitive to the applied value for l_{max} and to the matching of the local and nonlocal closures at the plume's downwind boundary, where the nonlocal heat flux (see Equation 18) is below its assumed critical value F_{crit}. For narrow leads ($L \ll D$), for which the L08 closure is derived, F_{crit} is reached downstream of the lead so that such a discontinuity was not simulated (see L08). For wide leads (e.g., $L = 5$ km), the nonlocal scheme is not used any more starting already at $y < L$ so that the results resemble those of the local scheme for the region downstream of the lead. As Figure 5a shows, this holds also for a much smaller F_{crit} than the value assumed by L08, for example, $F_{crit} = 0.1$ Wm^{-2}.

Also the vertical velocity variances $\overline{w'^2}$ (Equation 26) approach zero already at $y < L$ (Figure 5b). Consequently, the simulated total heat flux above the second half of the lead is mainly due to local effects when the L08 closure is applied to wide leads. Furthermore, the convection does not penetrate into the inversion causing less entrainment than with LES. This prevents the stabilization of the downstream ABL and stratification remains unstable (Figure 4d).

As expected, the patterns of horizontal wind speed and momentum fluxes are similar to the patterns obtained with the local closure (Figures 4f and 4h) since L08 use a nonlocal approach for heat but a local closure for momentum (section 2.2.2). Thus, although small improvements are obvious with the L08 scheme, also these results show discrepancies to the LES when L exceeds the lead width considered by L08 (see also Figure S1).

5. New Turbulence Parametrization

5.1. Principles and Derivation

The L08 parametrization was developed for narrow leads ($L \approx 1$ km) and, thus, it is not surprising that the application outside of its range of applicability to the much wider lead ($L = 5$ km) results in the discussed

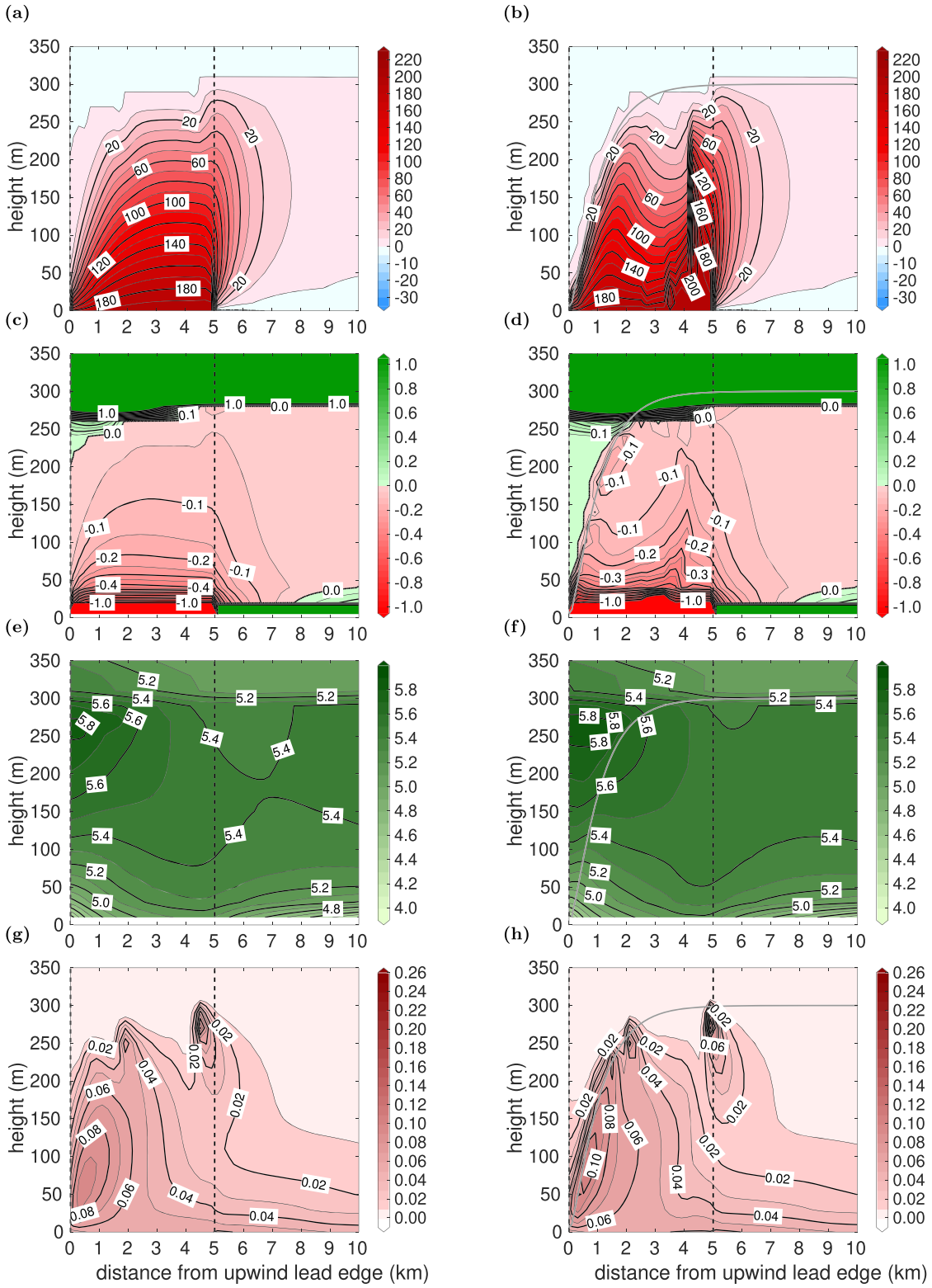

Figure 4. Results obtained with METRAS using the local mixing-length closure (left column) and using the L08 parametrization (right column) for case L5c-U5 of heat flux in Wm^{-2} (a, b), vertical potential temperature gradient in K per 100 m (c, d), horizontal wind speed in ms^{-1} (e, f), and vertical momentum flux in Nm^{-2} (g, h). The position of the lead is between 0 km and the vertical dashed black line. The distance between heat flux contour lines is 5 Wm^{-2} for negative fluxes. The solid gray lines in the right column show the upper IBL height according to Equation 11. Corresponding LES results are shown in Figures 2c, 2d, 3c, and 3d.

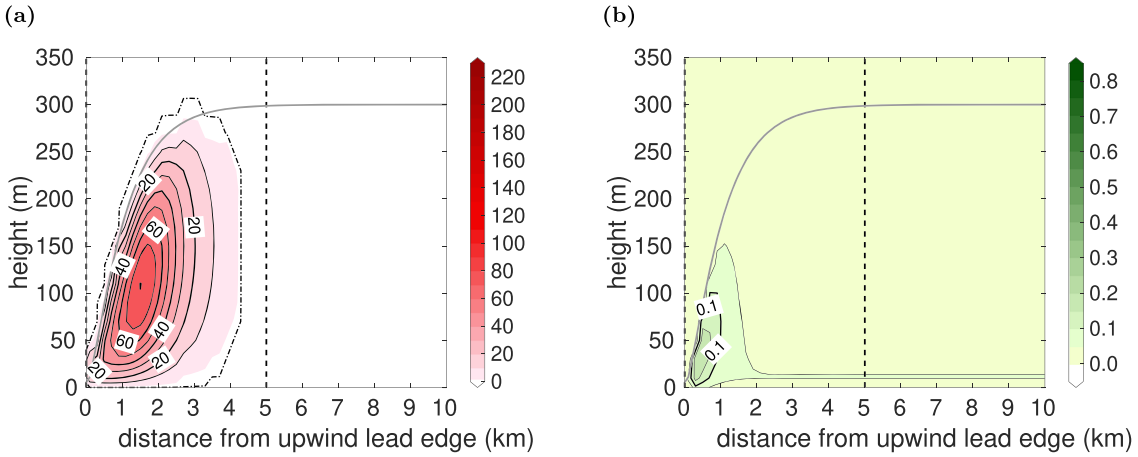

Figure 5. Results of the nonlocal heat flux $F_{h,nl} = \rho_0 c_p K_h \Gamma$ in Wm^{-2} (a) and vertical velocity variance $\overline{w'^2}$ (Equation 26) in $\mathrm{m}^2\mathrm{s}^{-2}$ (b) obtained with METRAS using the L08 parametrization for case L5c-U5. In (a), the dashed-dotted black contour line denotes where $F_{h,nl} = 0.1\,\mathrm{Wm}^{-2}$ and colored contour levels start at $F_{h,nl} = 2\,\mathrm{Wm}^{-2}$. In (b), the solid gray line shows the upper IBL height according to Equation 11.

difficulties. Therefore, in the following, we present a modified version of the L08 parametrization that will avoid the discussed drawbacks. It includes L as a parameter and is as robust against variations of the upstream wind speed U, ABL height z_i, and sea ice-lead surface temperature differences as the original closure. The basic ideas, namely, the separation of the turbulence regimes inside and outside the plume regions and the assumption of decaying turbulence downstream of the lead, remain unchanged. However, in the L08 parametrization, the decay of turbulence starts for simplicity already at the lead's upstream edge, while in our new version, we assume fully developed convection above the lead and apply a decay function only over sea ice. Thus, we will adjust the convective velocity scale $w_l(y)$, which has consequences also for the IBL height $\delta(y)$. For reasons that are explained below, we modify also the convective temperature scale θ_l and the parametrization of decaying convection on the lead's downstream side. A similar approach has been proposed by Gollnik (2008), but his determination of the parameters is based on rough estimations compared to the methods described here (see below). Furthermore, based on an LES study of decaying convection (Nieuwstadt & Brost, 1986), we consider two different decay length scales, one for the decay of vertical wind fluctuations, D_w, and one for the decay of temperature fluctuations, D_θ (see Appendix A1). Unlike L08 and Gollnik (2008), we apply a nonlocal closure also for the momentum fluxes.

The basic equations of the new parametrization are the same as in L08 (Equations 5,16, and 18). However, unlike L08, we account for the different behavior above and downstream of the lead by defining the vertical velocity scale as

$$w_l(y) = \begin{cases} c(\delta_l(y)B_l)^{1/3}, & 0 \le y \le L \\ c(\delta_l(y)B_l)^{1/3}\exp\left(\dfrac{L-y}{D_w}\right), & y > L, \end{cases} \tag{19}$$

where D_w is the decay length scale for vertical wind fluctuations (similar to D in L08) and where c is a parameter. By this definition, the decay of w_l starts over the downstream lead edge rather than over the upstream edge as in L08. Moreover, the determination of both D_w and c differs from L08 (see below). Besides these differences, the second line of Equation 19 results in the limit $L \to 0$ in the same equation as in L08.

As L08, we consider Equation 10 to determine the upper IBL height $\delta(y)$ assuming $\delta(y) = 0$ at the lead's upstream edge ($y = 0$) as lower boundary condition. To arrive at the final equation for $\delta(y)$, we use Equation 10, but limit $\delta(y)$ to z_i. We obtain after integration of Equation 10 with Equation 19

$$\delta(y) = \begin{cases} \min\left(z_i,\ \left(\frac{2aB_l^{1/3}}{3\ U}y\right)^{3/2}\right), & 0 \le y \le L \\ \min\left(z_i,\ \delta_L\left(1+\frac{D_w}{L}\left(1-\exp\left(\frac{L-y}{D_w}\right)\right)\right)^{3/2}\right), & y > L \end{cases}, \tag{20}$$

where δ_L is defined as

$$\delta_L = \left(\frac{2a\,B_l^{1/3}}{3\quad U}L\right)^{3/2}, \tag{21}$$

with the parameter a defined as described below. This formulation guarantees continuity of $\delta(y)$ at $y = L$. In this work, the limit $\delta(y) \ge z_i$ is reached for $y < L$ in all cases with $L = 5$ km and $L = 10$ km (wide leads). Equation 20 is valid for any possible value of L. For $L \to 0$, also $\delta(y) \to 0$. For $L \to \infty$, two cases have to be regarded. If $\delta_L < z_i$, $\delta(y) \to \delta_L$. If $\delta_L = z_i$, also $\delta(y) = z_i$.

For parametrizing the decaying convection, unlike L08, we do not assume that $\delta(y)$ approaches z_i for $y \to \infty$, if the limit $\delta(y) \ge z_i$ is not reached at $y \le L$. Not only for wide leads, $\delta(y)$ reaches z_i anyway already at $y < L$ but also for narrow leads, the convection reaches z_i in almost all cases between approximately $1 < y < 8$ km (see entrainment fluxes in LES results of L08, their Figures 3 and 8). Thus, we cannot obtain the decay length scale D_w from Equation 20 as in L08. Our modified approach for this parameter is explained in Appendix A1, and we obtain

$$D_w = d_w \cdot U\frac{z_i^{2/3}}{B_l^{1/3}}, \tag{22}$$

where d_w is a parameter (see Appendix A1).

Unlike L08, we apply an exponential decay function also for the convective temperature scale θ_l to account for the decay of temperature fluctuations at $y > L$. We obtain

$$\theta_l(y) = \begin{cases} \frac{\overline{w'\theta'}|_s}{w_l(y)}, & 0 \le y \le L \\ \frac{\overline{w'\theta'}|_s}{w_l(y)}\exp\left(\frac{L\ -\ y}{D_\theta}\right), & y > L \end{cases}, \tag{23}$$

where D_θ is the decay length scale for temperature with

$$D_\theta = d_\theta \cdot U\frac{z_i^{2/3}}{B_l^{1/3}}, \tag{24}$$

where d_θ is a parameter (see Appendix A1). In Figure 6, we illustrate the necessity of using Equation 23 instead of Equation 8 by showing the effect of both equations on the nonlocal term Γ, exemplarily for case L5c-U5. The dashed lines in Figure 6 show that Γ would increase for $y > L$ especially in the upper part of the ABL if we did not consider the second line of Equation 23. This would result in unrealistically increasing heat fluxes at $y > L$, which contradicts also LES (Figure 2, left column).

Downstream of the lead, we adopt the assumption of L08 that mixing far away from the plume is dominated by local effects. Thus, we also take $\delta_d(y)$ as switching line. Unlike L08, we set $F_{crit} = 0.1\ \mathrm{Wm}^{-2}$ since compared with LES the simulated entrainment was underestimated using the original value (not shown). This new value was found by a systematic variation of F_{crit} in small steps and comparing results for all cases with LES. The modification of the closure has consequences also for the values of the other unknown parameters.

Since the new closure assumes no decay of turbulence over the lead, values obtained for the convective velocity scale w_l with this closure are higher than with the corresponding Equation 9 of the L08 closure. A higher

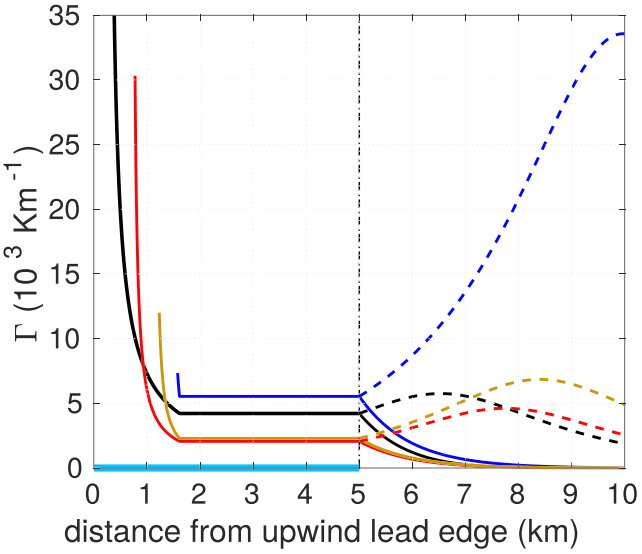

Figure 6. METRAS results of the nonlocal term Γ (in 10^3 Km^{-1}) in the new parametrization (section 5.1) at different heights (colored) obtained with either Equation 8 (dashed) or Equation 23 (solid) for the convective temperature scale θ_l at $y>L$. Black: $z=20$ m, red: $z=100$ m, brown: $z=200$ m, and blue: $z=290$ m. Case is L5c-U5, and the lead is between 0 and 5 km distance.

value of w_l results in a smaller inclination of the plume. Thus, the parameters c and finally a, which also determine the plume inclination, need to be lowered relative to the values $c=1.6$ and $a=2.3$ used by L08, when a similar quality of agreement shall be reached as for the L08 closure. With our assumption that convection over a lead is similar to convective conditions over homogeneous surfaces, we obtain $w_l=w_*$ if the limit $\delta(y)=z_i$ is reached above the lead (see Equations 6 and 19); hence, we set $c=1$. This value was confirmed by determining c with the help of LES results (see Appendix B1). c might depend on L, but a comparison with LES showed that this dependence can be neglected and, thus, the value $c=1$ is applicable for the cases considered here.

For a_e and a_m, we apply the same ranges as determined by L08 (section 2.2.2). With $c=1$ and $a=a_e a_m c$, we obtain $a=1\pm0.6$, which is also lower than in L08. Based on the simulated plume inclinations, our results agree best with LES if we set $a=1.2$ (see also Table B1 in Appendix B1 and Figures S4 and S5).

We change also b, which determines the magnitude of Γ (Equation 18). Due to the application of smaller values for c and a, results obtained with the value of L08 ($b=0.6$) disagree with LES (see Figure S2), namely, due to an underestimated counter-gradient transport. We obtain the best agreement with LES, if we set $b=2$. This agrees perfectly with the value proposed originally for b used in Γ by Holtslag and Moeng (1991) on the basis of LES for convection over homogeneous surfaces and whose approach forms the basis for our parametrization. For d_w and d_θ, we obtain $d_w\approx1.7$ and $d_\theta\approx0.51$ also based on LES (see Appendix A1).

Regarding the momentum fluxes, we found that results obtained with a nonlocal instead of a local approach for the eddy diffusivity K_m agree better with LES. We obtain K_m following Lüpkes and Schlünzen (1996), where we apply the corresponding equation only inside the convective plume:

$$K_m = K_h\left(\frac{\Phi_h|_{z_p}}{\Phi_m|_{z_p}} + b\frac{w_l(y)u_*\kappa z_p}{\Phi_m|_{z_p}\overline{w'^2}|_{z_p}\delta(y)}\right), \quad \delta_d(y)<z\le\delta(y), \tag{25}$$

where Φ_m is the Monin Obukhov similarity function for momentum and $\overline{w'^2}$ is the vertical velocity variance, which is parametrized as in L08 via

$$\overline{w'^2} = 1.6u_*^2\left[(1-Z)^{3/2} + 0.593S^3Z(1-0.9Z)^{3/2}\right]^{2/3}, \tag{26}$$

with S and Z calculated via Equations 14 and 15. Originally, Equation 26 was derived by Holtslag and Moeng (1991) for horizontally homogeneous convection based on LES and observations.

5.2. Results for Wide Leads

Simulation results of METRAS obtained with the new closure (section 5.1) are discussed in the following, mainly for the same cases as in section 3.

5.2.1. Cold Cases

Basically, the simulated patterns of both heat fluxes (Figure 7, left column) and ABL stratification (Figure 7, right column) agree well with the corresponding LES results (Figure 2). Using the new closure, the overall shapes of the convective plumes, the positions of the maximum heat fluxes, and the magnitudes of the simulated entrainment fluxes do not differ considerably from the LES results. Also the maximum values of heat fluxes at $z=100$ m and $z=200$ m agree well with the LES values (Table 1). Furthermore, the simulated plume boundaries downstream of the lead are clearly visible, which was not the case in the METRAS results using the local or the nonmodified L08 closure (Figures 4a and 4b). Thus, in contrast to those results, a slightly stable stratification is now simulated downstream of the lead for all cases in good agreement with

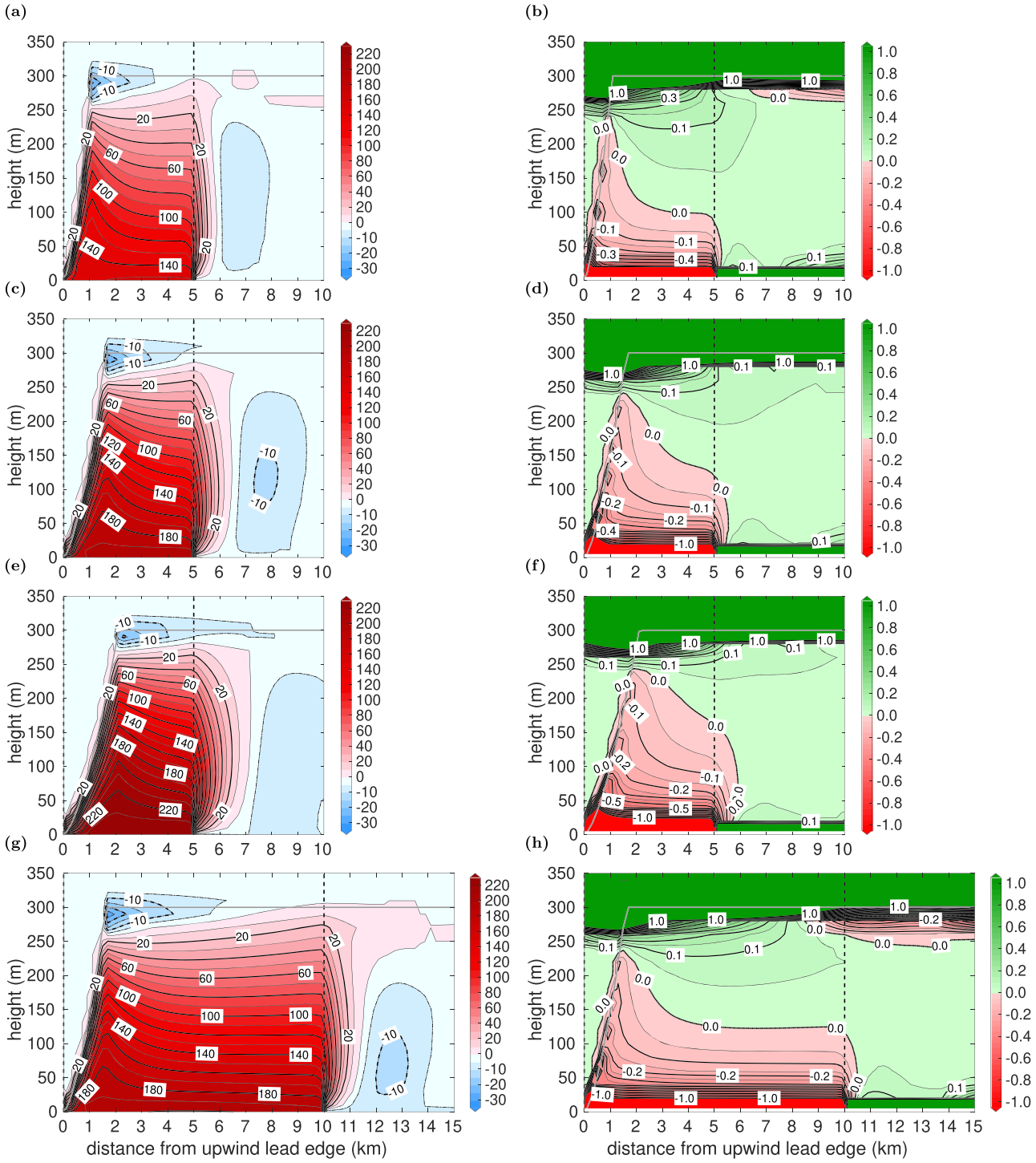

Figure 7. Heat flux (Wm^{-2}) and vertical potential temperature gradient (K per 100 m) for the same cases as for the LES results in Figure 2, but obtained with METRAS using the new parametrization (section 5.1). The solid gray lines show the upper IBL height according to Equation 20.

the LES results. Furthermore, similar effects as simulated with LES are shown for increasing wind speed (Figures 7a, 7c, 7e) and lead width (Figure 7g).

Some details are, however, not reproduced with METRAS using the new closure. For instance, an increase in ABL thickness with increasing fetch over the lead is not as pronounced as with LES. Furthermore,

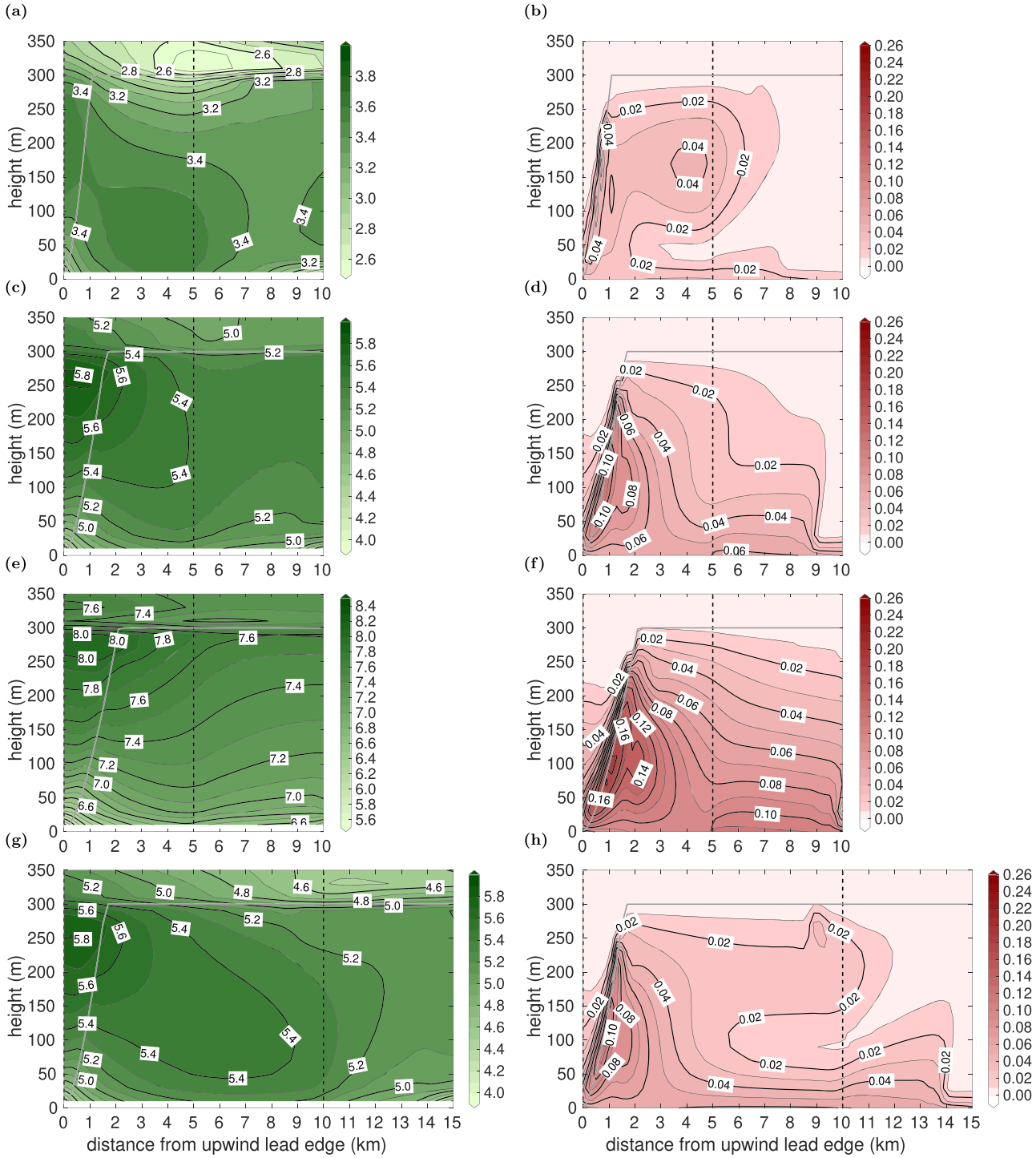

Figure 8. Results obtained with METRAS using the new parametrization as in Figure 7, but horizontal wind speed in ms^{-1} (left column) and vertical momentum flux in Nm^{-2} (right column) are shown. The corresponding LES results are shown in Figure 3.

fetch-dependent positions of the maximum heat fluxes above the lead are not simulated and entrainment is weaker.

In all four cases an LLJ is simulated with its core in the upper third of the ABL near the lead's upstream edge (Figure 8, left column) and the core region is also inclined towards the surface with increasing fetch. A clear weakening of the LLJ over the lead center is shown in all cases. Especially for case L5c-U3, a secondary

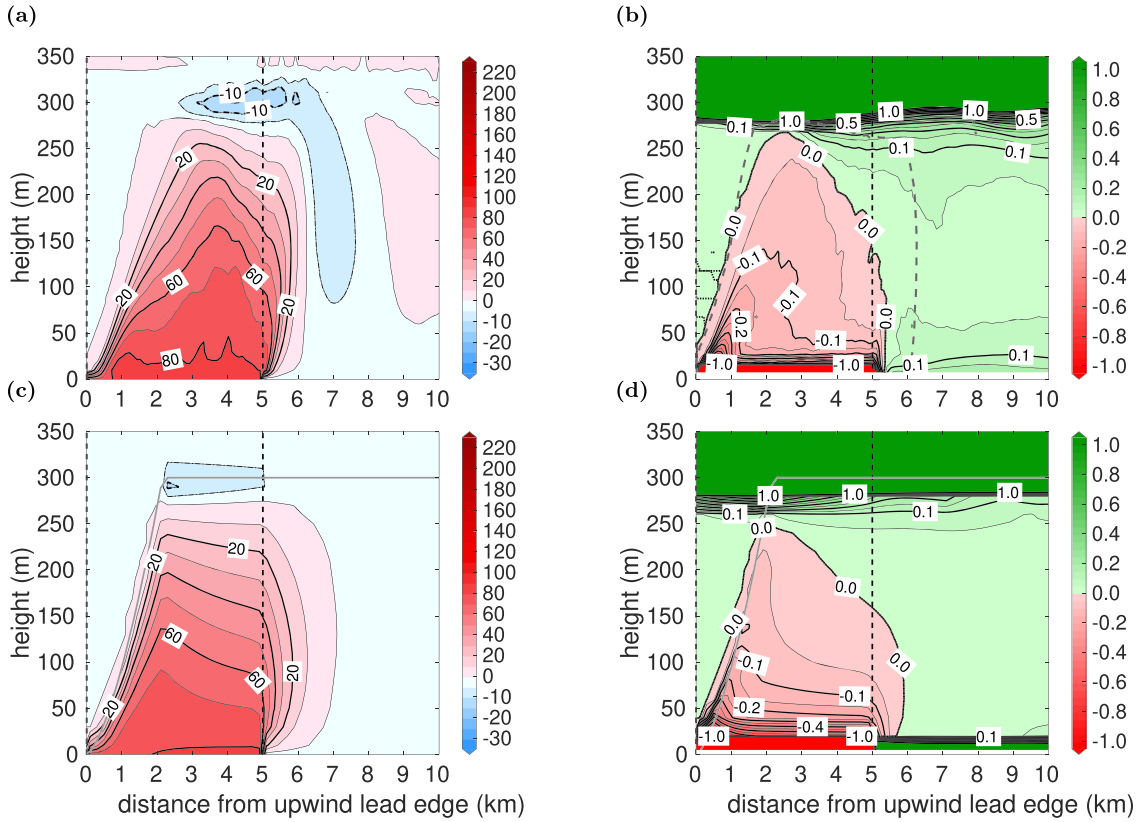

Figure 9. (a, b) LES results as shown in Figures 2c and 2d and (c, d) results obtained with METRAS using new parametrization (section 5.1) as shown in Figures 7c and 7d, but results of heat flux in Wm^{-2} (left column) and vertical potential temperature gradient in K per 100 m (right column) are shown for case L5w-U5.

maximum is simulated at $z = 50$ m above the second half of the lead (Figure 8a). Downwind of the convective plume, in most cases a regeneration of the LLJ is shown. These simulated wind field structures agree well with the LES results (Figure 3, left column). Note that similar effects have been measured by Tetzlaff et al. (2015), which supports both our LES results and considering nonlocal effects in the new parametrization also for K_m. Only for case L5c-U7 (Figure 8e) the destruction and regeneration of the LLJ obtained with the new parametrization are not as pronounced as with LES.

Unlike L08, we consider also momentum fluxes (Figure 8, right column). Their general pattern and the positions of their maxima near the upstream edges are simulated in fair agreement with LES results (Figure 3, right column) if the new closure is used. However, the maxima simulated with METRAS are slightly less pronounced than with LES. Furthermore, except for case L5c-U3, the secondary maxima near the lead's downstream edge are not reproduced and the downstream decay seems to be too weak as compared to LES.

5.2.2. Warm Cases

In Figure 9, heat flux and stratification patterns from both models are shown for case L5w-U5. Thus, we consider the effect of strongly increased inflow temperature. The LES results (Figures 9a and 9b) show that the smaller temperature difference in case L5w-U5 in comparison to L5c-U5 (Figures 2c and 2d) has several effects on the flow characteristics over the lead: weaker heat fluxes, increased plume inclination, and slightly less pronounced stratification downstream of the lead. Basically, the corresponding METRAS results obtained with the new parametrization (Figures 9c and 9d) agree well with the LES. This holds for both heat fluxes and ABL stratification. Again, differences concern mainly the positions of the maximum heat fluxes and the magnitude of the entrainment fluxes.

5.2.3. Variance of Vertical Velocity

Basically, also results of the vertical velocity variance $\overline{w'^2}$ (Equation 26) obtained with the new closure agree with LES (Figure 10). With LES, the highest values are simulated in the center of the convective regions for

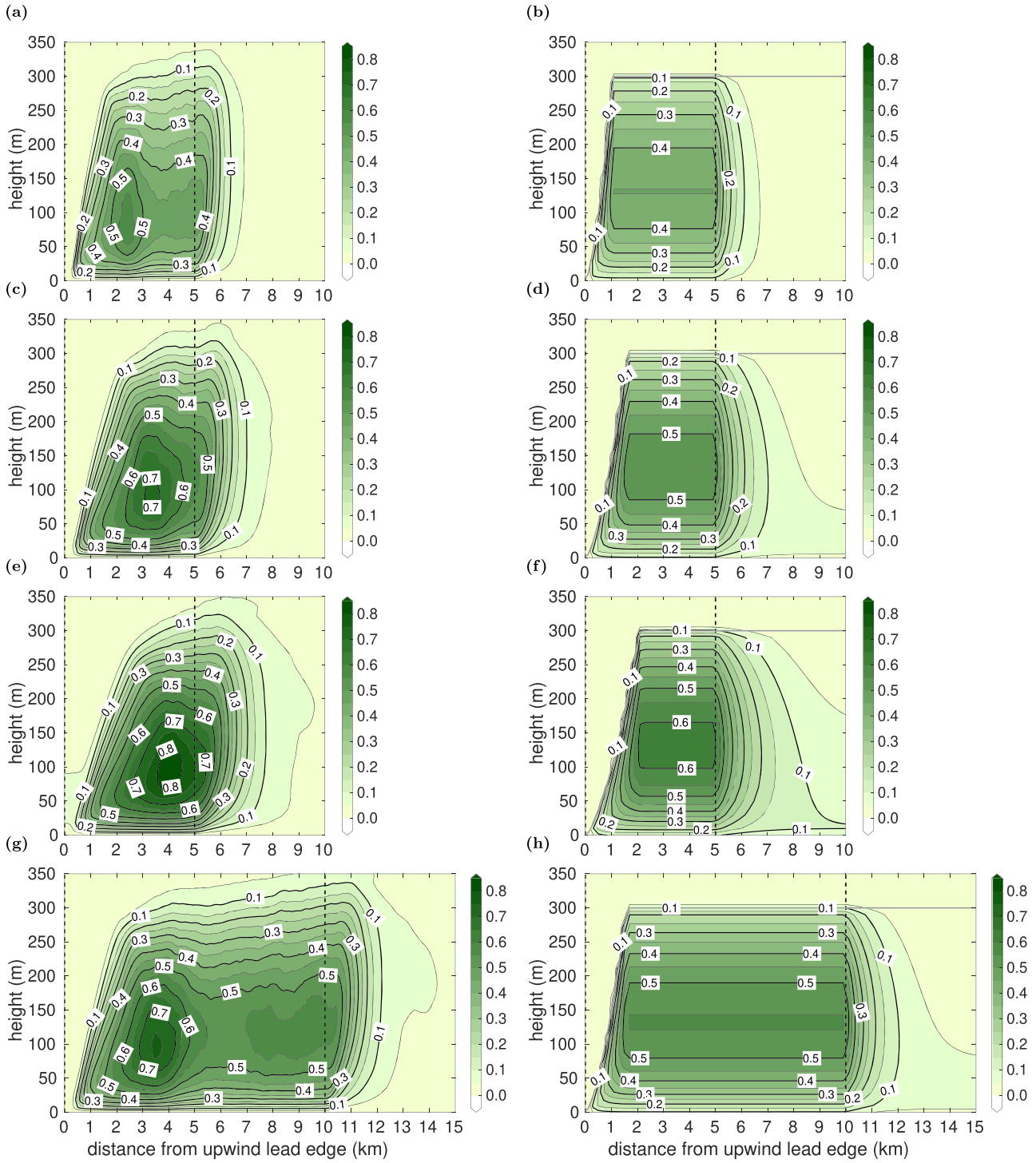

Figure 10. Vertical velocity variance $\overline{w'^2}$ (m^2s^{-2}) from LES (left column) and METRAS using the new parametrization from section 5.1 (right column) for L5c-U3 (a, b), L5c-U5 (c, d), L5c-U7 (e, f), and L10c-U5 (g, h). In the right column, the solid gray lines show the upper IBL height according to Equation 20.

all cases and downstream of the lead $\overline{w'^2}$ decreases (Figure 10, left column). This is well reproduced with METRAS using the new closure (Figure 10, right column). Differences between the results of both models concern mainly the horizontal inhomogeneity of $\overline{w'^2}$ in the convective core regions, which is especially shown in the LES of the cases L5c-U3 and L10c-U5 (Figures 10a and 10g), but not reproduced with the

new closure (Figures 10b and 10h). Furthermore, with LES, the maxima of $\overline{w'^2}$ are up to 40% higher. Downstream of the lead, the decrease of $\overline{w'^2}$ starts at $y = L$ near the surface but further downstream towards z_i (Figure 10, left column), which is also not reproduced with the new closure (Figure 10, right column). This result is related to the same disagreement in the heat and momentum fluxes (Figure 7, left column; Figure 8, right column).

5.3. Results for Narrow Leads

Within the range of our applied wind regimes and temperature differences (see Table 1), the convective plume over narrow leads does not penetrate into the inversion already above the lead. Thus, in contrast to wide leads, for narrow leads the second line of Equation 20 is used for $\delta(y)$. We performed L1c-U3, L1c-U5, L1c-U7, and L1w-U10 simulations as in L08 (their Tables 1 and 2). To ensure comparability, we show heat flux patterns and potential temperature distributions for a lead 10 km downstream of another lead (Figure 11). New LES results of those scenarios are shown in Figure S3. Furthermore, LES and METRAS results with both nonlocal closures are presented for a scenario with $L = 0.5$ km in Figure 12 (case L0.5c-U5, Table 1).

5.3.1. Lead Width: 1 km

As Figure 11 shows, the simulated patterns of both heat fluxes and potential temperature agree again well with our LES results (Figure S3). The latter differ only slightly from those shown by L08 (their Figures 3 and 8, lower row), but convection is already fully resolved by the LES close to the upstream lead edge, which results in a more linear increase of the IBL than in the L08 LES result using lower resolution. METRAS results for $L = 1$ km obtained with the new closure agree also well with the results obtained with the original L08 closure (see Figures 6 and 9, lower row of L08), especially plume inclinations and heat flux patterns. Also, the simulated maximum heat fluxes at $z = 100$ m and $z = 200$ m agree well with the corresponding values from LES, except for case L1c-U3 where our results are about 25 Wm^{-2} higher (Table 1). A clear improvement is shown in our results concerning the position of the entrainment fluxes as compared to the METRAS results obtained with the L08 closure (see L08, their Figures 6 and 9, left columns).

5.3.2. Lead Width: 0.5 km

According to Figure 12, also for leads of width $L = 0.5$ km results obtained with the new parametrization (Figures 12e and 12f) agree well with LES (Figures 12a and 12b), mainly concerning plume inclination and downstream stratification. The plume inclination agrees with LES also if we use the closure of L08 (Figures 12c and 12d), but the magnitude of heat fluxes downstream of the lead disagrees. This is due to an overestimation of the nonlocal heat flux with the L08 closure (not shown).

5.4. Sensitivity Studies

5.4.1. Variation of parameters

The sensitivity of our results was tested with additional simulations using alternative values for the tunable parameters in the new parametrization. For b, we considered simulations of case L5c-U5 with the values applied by Lüpkes and Schlünzen (1996) ($b = 3$) and by L08 ($b = 0.6$), respectively. With $b = 3$, maximum heat fluxes at $z = 100$ m and $z = 200$ m are overestimated by about 25 Wm^{-2} with respect to LES and the stability especially in the upper part of the mixed layer is overestimated, too (Figures S2c and S2d). With $b = 0.6$, the magnitude of nonlocal heat fluxes especially in the upper part of the mixed layer is underestimated. At, for example, $z = 200$ m, the maximum heat flux is then more than 40 Wm^{-2} lower than with LES and, in contrast to LES, the downstream ABL stratification is slightly unstable (Figures S2a and S2b). Furthermore, with $b = 0.6$, positive fluxes are obtained in the downwind mixed layer in contrast to strong negative fluxes with $b = 3$, which are even stronger than with LES. This is caused by a redistribution of heat in the ABL by adjusting b, where an increase of b causes lower temperatures near the surface and higher temperatures near the ABL top (see also L08).

Due to our assumption $w_l = w_*$ for convection that reaches z_i already at $y < L$, we set $c = 1$ (Equation 19), and we applied this also for narrow leads (section 5.1). Thus, $c \neq 1$ would mean that we assumed convection over leads to be stronger or weaker as compared to homogeneous conditions, on average. This would cause a drawback regarding our basic assumption formulated in section 5.1. Furthermore, L08 showed that a variation of c by ± 25 % would have only small effects on the fluxes. For this reason and also because the assumption $c = 1$ is supported by our LES results (Appendix B1), we did not consider any variations of c.

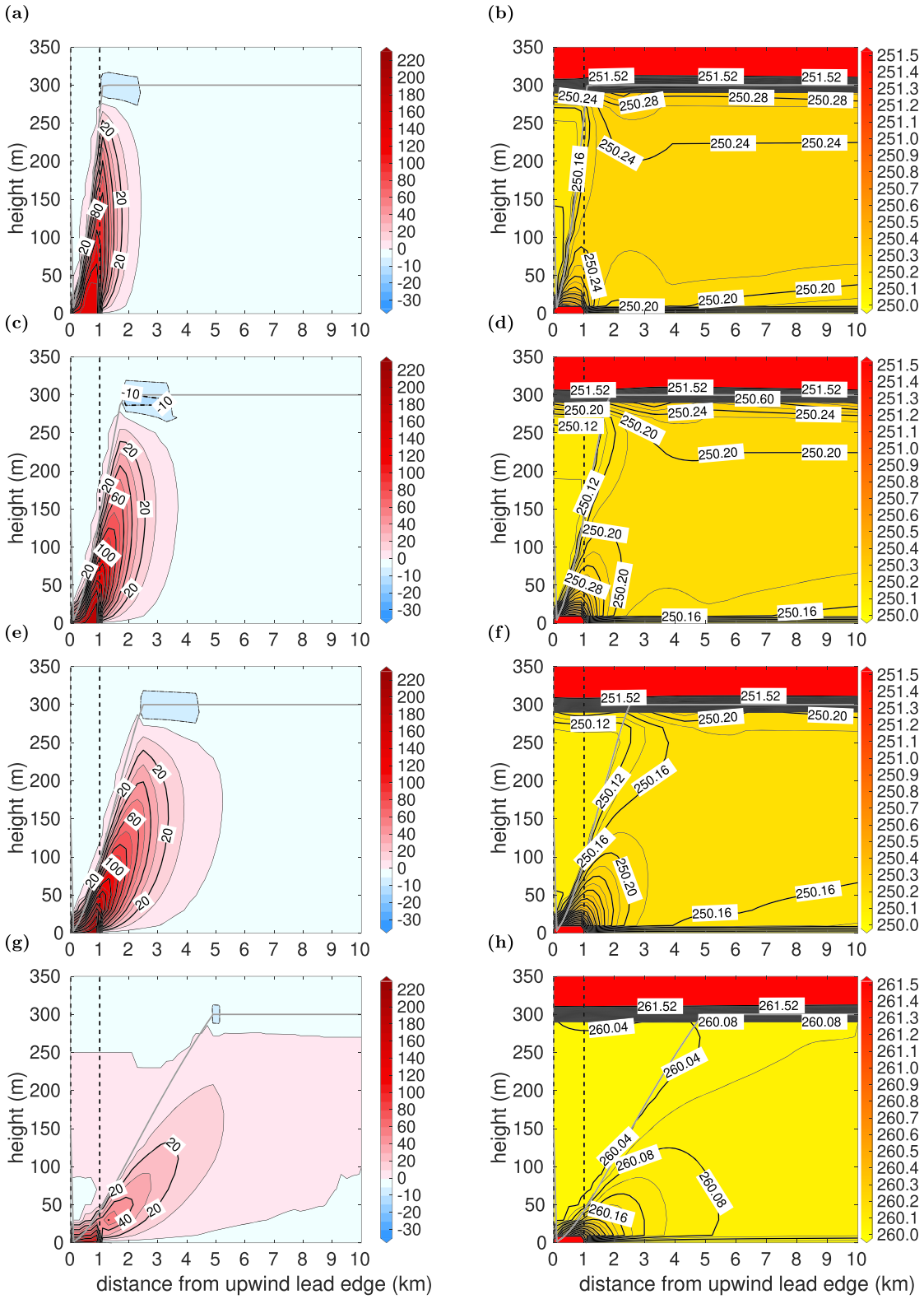

Figure 11. METRAS results obtained with the new parametrization (section 5.1) of heat flux in Wm^{-2} (left column) and of potential temperature in K (right column) for the cases L1c-U3 (a, b), L1c-U5 (c, d), L1c-U7 (e, f), and L1w-U10 (g, h). The position of the lead is between 0 km distance and the dashed vertical black line. The spacing between heat flux contour lines is 5 Wm^{-2} for negative fluxes. The solid gray lines show the upper IBL height according to Equation 20. Note the different temperature scale in (h). Corresponding LES results are shown in Figure S3 and in L08 (their Figures 3 and 8, lower row).

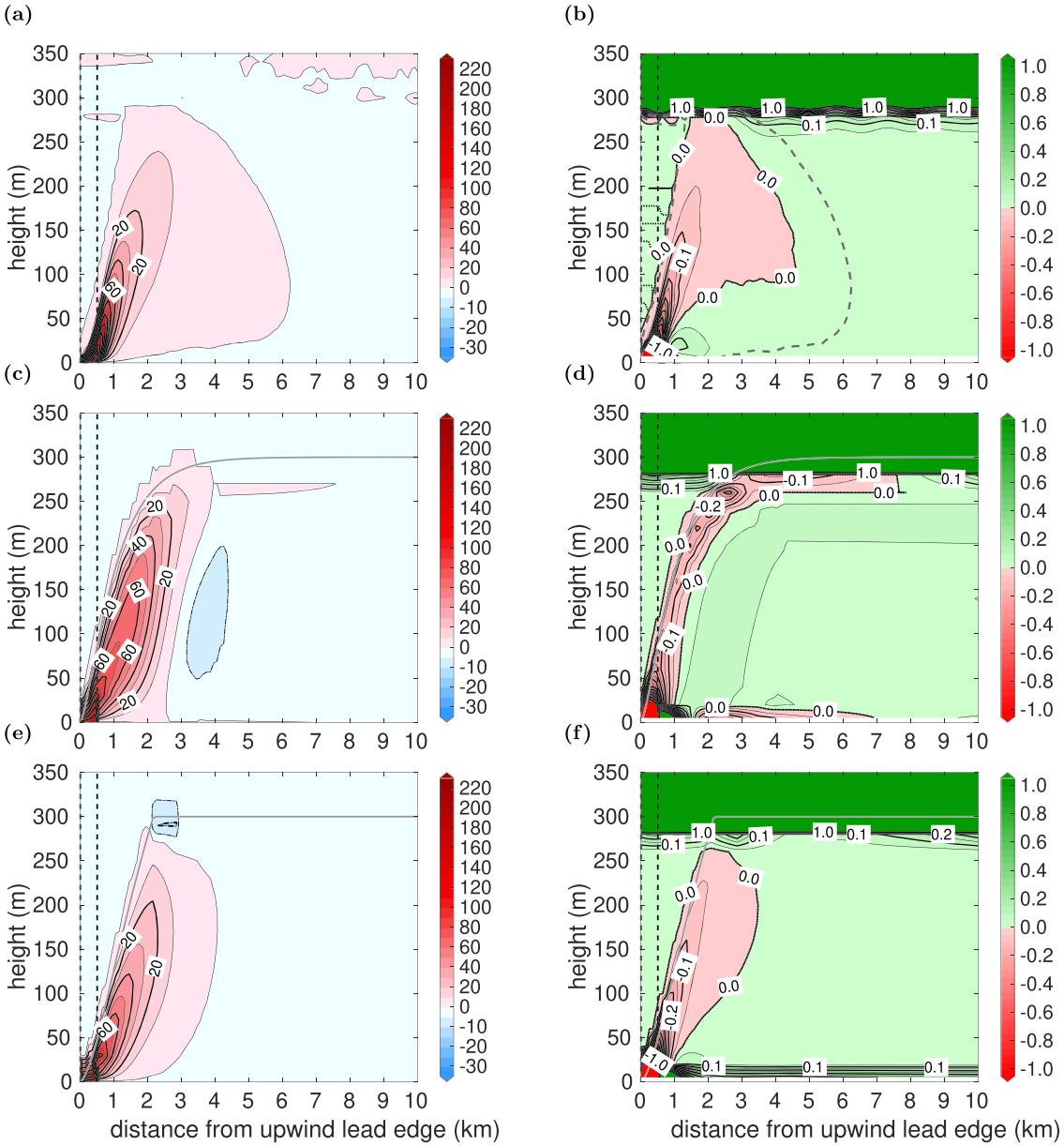

Figure 12. Heat flux in Wm^{-2} (left column) and vertical potential temperature gradient in K per 100 m (right column) of case L0.5c-U5 obtained with LES (a, b), METRAS using the L08 parametrization (c, d), and METRAS using the new parametrization from section 5.1 (e, f). The position of the lead is between 0 km distance and the dashed, vertical black line. The spacing between heat flux contour lines is 5 Wm^{-2} for negative fluxes. In (b), the area inside the dashed gray lines depicts the region of positive fluxes inside the convective plume. In (c) and (b), the solid gray lines show the upper IBL height according to Equation 11 and in (e) and (f) according to Equation 20.

A variation of a has a strong effect on the plume inclination, whereas the effects on the downstream ABL characteristics are negligible (not shown). Our results show that, especially for weak wind, the plume inclinations are slightly underestimated with $a = 1.2$ for both wide (Figure 7a compared to Figure 2a) and narrow leads (Figure 11a compared to Figure S3a); hence, maximum heat fluxes at a certain height are overestimated (Table 1). However, for example, with $a = 1$, plume inclinations for higher wind speeds would then be overestimated (not shown). Therefore, our value for a can be seen as a compromise, where for the majority of our scenarios plume inclinations obtained with the new closure agree with LES (see also Appendix B1).

5.4.2. Momentum Transport

Our application of a nonlocal parametrization of K_m (Equation 25) causes an improved agreement with LES as can be seen by comparing the corresponding results in Figure 8 (METRAS with the new closure) and

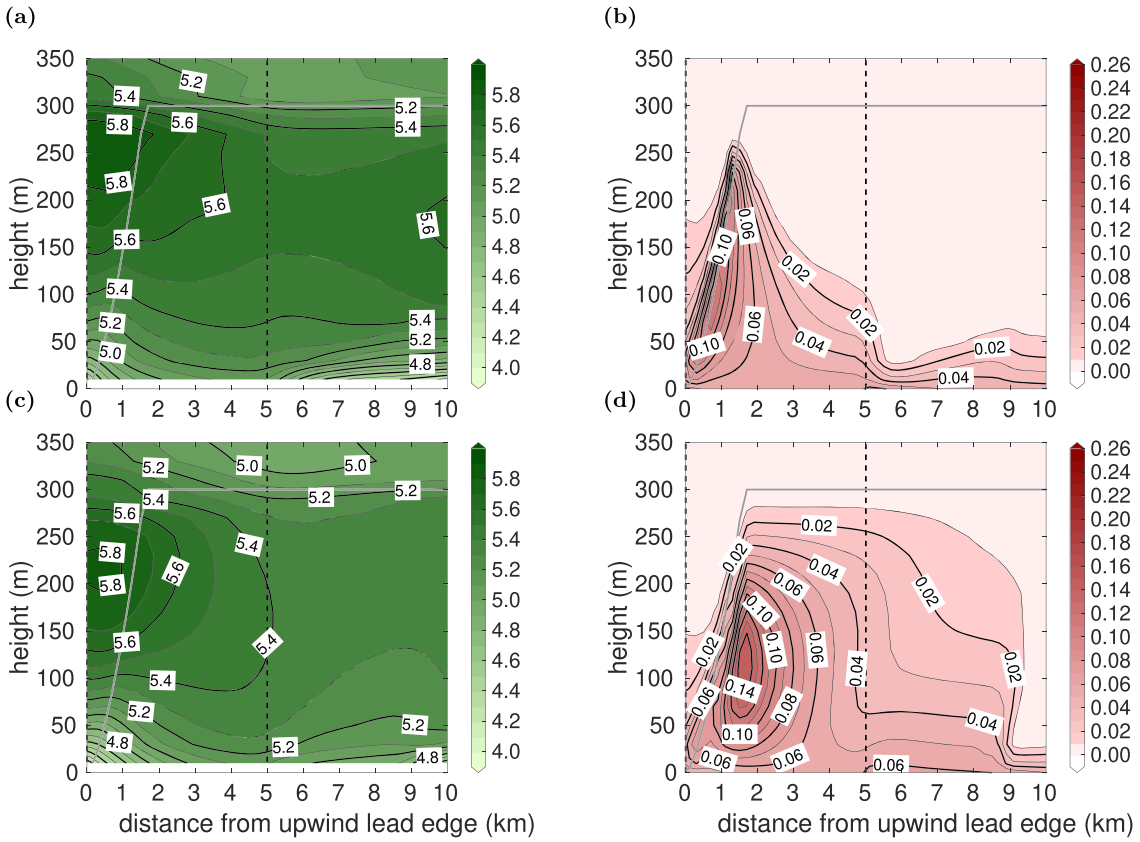

Figure 13. Wind speed (ms^{-1}) and momentum fluxes (Nm^{-2}) for case L5c-U5 obtained with METRAS using the new parametrization for heat transport as in Figures 8c and 8d. For panels (a) and (b), a local closure is applied for the eddy diffusivity for momentum (Equation 3 instead of the nonlocal parametrization in Equation 25 used for panels (c) and (d)). In (c) and (d), the maximum mixing length l_{max} (see Equation 3) is set to 15 m instead of $0.15z_i$. See Figures 3c and 3d for the corresponding LES results.

Figure 3 (LES). Obviously, when the local approach is used for K_m only (Figure 13a), the destruction of the LLJ with increasing fetch over the lead is not as effective as compared to the simulation with nonlocal K_m (Figure 8c) and to LES (Figure 3c). Furthermore, momentum fluxes in the upper downstream half of the ABL over the lead are smaller than with LES (Figure 13b).

Results of a simulation using a nonlocal approach for both K_h and K_m but with a maximum mixing length l_{max} lowered to 15 m instead of about 45 m resulting from $l_{max} = 0.15z_i$ are shown in Figures 13c and 13d. With $l_{max} = 15$ m, the LLJ position upstream of the lead is at $z \approx 220$ m (Figure 13c), which is about 50 m lower than obtained with $l_{max} = 0.15z_i$ (Figure 8c) and with LES (Figure 3c). Regarding the maximum momentum transport, the value obtained with $l_{max} = 15$ m agrees better with LES (Figure 3d) than the value obtained with $l_{max} = 0.15z_i$ (Figure 8d). However, the position of that maximum is rather at $0.4z_i$ than at $0.1z_i$ as in LES, and it is simulated further downstream than with LES.

6. Discussion

6.1. Importance of Nonlocal Closure and *L* as Parameter

First, our results clearly show the importance of using fetch-dependent nonlocal turbulence closures for non-eddy-resolving atmospheric models to simulate the characteristics of lead-generated convection in the ABL, properly. Results and drawbacks obtained with the used local closure can be considered as representative in the sense that also the use of a more sophisticated TKE-closure cannot improve results as long as the nonlocality of heat fluxes is not reproduced.

Second, we stress that with our modification of the L08 closure the simulated patterns agree well with LES for different lead widths L. The nonlocal L08 closure was developed for narrow leads and, indeed, we showed

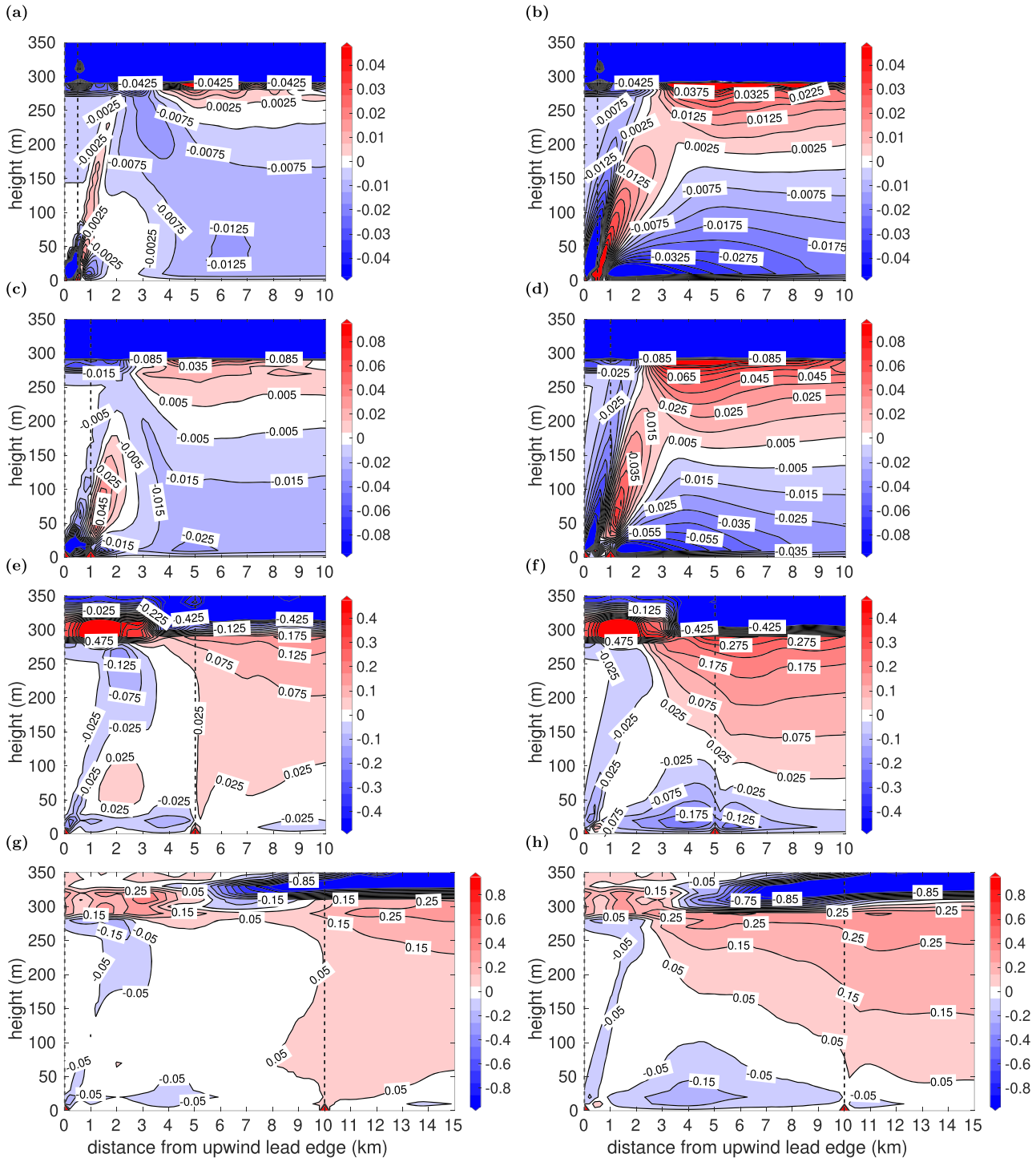

Figure 14. Differences in potential temperature (K) between LES and METRAS using the new parametrization from section 5.1 (left column) and the local closure from section 2.2.2 (right column). Cases are L0.5c-U5 (a, b), L1c-U5 (c, d), L5c-U5 (e, f), and L10c-U5 (g, h). The position of the lead is between 0 km and the vertical dashed black line. Note the different color scales.

drawbacks, especially for wide leads. The main step for an improvement of the L08 closure was to assume that the decay of turbulence starts at the downstream lead edge and not over the lead as in L08. Compared with LES, this is still a simplification because LES shows that the position of decay is height-dependent. Nevertheless, our approach allowed the introduction of the lead width L as a parameter in our

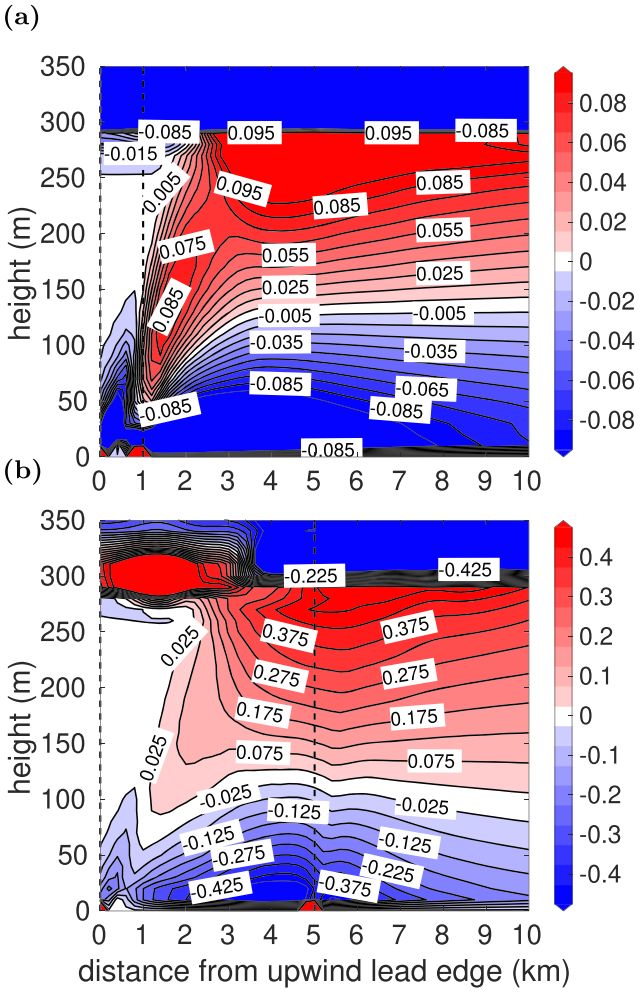

Figure 15. Differences in potential temperature (K) between LES and METRAS using the local closure as in Figure 14, but for the maximum mixing length $l_{max} = 0.007u_*/f$ is applied based on Blackadar (1962) instead of $l_{max} = 0.15z_i$ as in Figure 14. Cases are L1c-U5 (a) and L5c-U5 (b). Note the different color scales.

parametrization, and despite the still simplified treatment of decay, results for wide leads improved considerably as compared with LES. Furthermore, we showed that for $L = 0.5$ km results obtained with the new parametrization agree also slightly better with LES than those with the nonmodified L08. This shows the importance of L in the parametrization.

Closures describing counter-gradient transport were designed for an improved representation of the temperature field. Thus, we show in Figure 14 the improvement achieved with the new nonlocal closure compared to results obtained with a local closure in terms of temperature deviations from the LES result. Note that we did not use the same contour lines and color scales in each case since ABL warming and, thus, the absolute temperature differences between LES and METRAS are larger for wide leads than for narrow leads. As Figure 14 shows, differences between LES and METRAS are smaller when the new nonlocal instead of the local mixing-length closure is used. This holds independent on the value of L.

Another interesting point is that the results on the downstream side of the plume agree perfectly with LES in almost all cases. For case L0.5c-U5 this concerns, for example, the region between $y = L$ and $y = 3L$, which means that our relatively rough approximation of the decay of turbulence is sufficient.

The approach proposed in section 2.2.2 for the maximum mixing length in the local closure results in a much larger value compared with the often used value based on Blackadar (1962), where l_{max} is proportional to the ratio of friction velocity and the Coriolis parameter. Basically, with the smaller value, METRAS results are much worse than those shown in all figures for the local closure. This causes also a larger temperature deviation from LES (Figure 15).

6.2. Methodological Limitations

Our assumption of two decay length scales to describe the decaying convection downstream of the lead is based on Nieuwstadt and Brost (1986), and LES results of, for example, case L5c-U5 support our approach (Figure A1b). Furthermore, Figure 10 shows that the decay rates for vertical velocity fluctuations agree well with LES also for the other cases with $L \geq 5$ km. Thus, the value we obtained for d_w by linear regression can be considered as reasonable. Similarly, results of $\overline{\theta'^2}$ for cases other than L5c-U5 might help to evaluate our assumed ratio $d_\theta/d_w = 0.3$.

Figure 10 (left column) also shows that the decay of vertical velocity fluctuations near the surface starts at $y = L$, but towards z_i, this decay starts further downstream. Moreover, $\overline{w'^2}$ seems to be highly inhomogeneous over the lead in the center of the ABL. Both features are not captured by the new closure since we had to assume horizontally homogeneous conditions for $\overline{w'^2}$ to avoid a discontinuity in $\overline{w'^2}$ at $y = L$ and, thus, also in the fluxes. This would occur due to the necessary assumption of y-independent $u_\star$ for $y > L$ in Equation 19. Thus, any improvement with respect to the y-dependence of $\overline{w'^2}$ does not necessarily improve the other results. Nevertheless, our results for $\overline{w'^2}$ with the new closure represent a clear improvement compared to results obtained with the nonmodified L08 closure (see Figure 5b for case L5c-U5) and even more with the local closure.

Regarding the derivation of the parameters, especially for a, a_e, and a_m, a more detailed study of the relations between w_e, w_{max}, and w_l for different wind regimes seems necessary. Furthermore, as L08, we also

neglected horizontal entrainment u_e since we focus on plumes with small inclination angles where $U \gg u_e$. However, particularly at low wind, u_e becomes more important (Deardorff & Peterson, 1980; Esau, 2007; L08). Thus, considering u_e for the derivation of $\delta(y)$ could lead to a better representation of the IBL growth over leads at small U.

Our LES results show that the penetrating convection plays a critical role regarding entrainment and ABL thickness. In principle, the fetch-dependent increase in ABL thickness (Figures 2c and 2g) agrees with results of the modeling studies from Glendening and Burk (1992) and Zulauf and Krueger (2003), who found L-dependent relations for the plume penetration height. In our microscale model results obtained with the new parametrization, both increase in ABL thickness and entrainment are, however, partly underestimated as compared to LES. Consequently, the downwind warming of the ABL obtained with the new parametrization is less pronounced than with LES, mainly near the inversion and especially for wide leads (Figure 14, left column). This drawback is mainly caused by assuming a fixed value for z_i also for $y>0$, which causes less entrainment and prevents an increase in ABL thickness. Therefore, to better capture the effects of penetrating lead-generated convection, considering a fetch-dependent z_i seems necessary. This is supported by observations from Tetzlaff et al. (2015) who found different values for upstream and downstream ABL thickness in case of penetrating lead-generated convection. Moreover, an explicit consideration of entrainment (e.g., Noh et al., 2003) could be implemented, which is, however, challenging.

The downstream distribution of the turbulent momentum transport obtained with the new parametrization shows two additional differences as compared to LES. Secondary maxima near the lead's downstream edge were not reproduced, and the downstream decay seems to be underestimated, except for case L5c-U3. The reason could be another nonlocal component in the momentum transport, which is not yet represented by the new closure.

Improvements might also be achieved with other approaches for the treatment of the convection in the non-eddy-resolving model. As a promising alternative to the application of Equation 5, the so-called eddy-diffusivity mass-flux scheme (EDMF, Siebesma et al., 2007) could be applied. Following Equation 5, the small-scale fluxes and those generated by larger convective structures depend on each other via K_h in both terms. The EDMF approach has the advantage that these fluxes form separate contributions. Tetzlaff (2016), who compared both approaches in a modeling study of cold air outbreaks, shows not only some advantages but also disadvantages of the EDMF approach. For example, modifications of the existing EDMF schemes are necessary with respect to the matching of fluxes at the top of the surface layer, especially for shallow boundary layers. Furthermore, we expect that the decay of turbulence downstream of the lead would require modifications of the EDMF closure.

7. Conclusions

Our main goal was to derive an improved parametrization of the turbulence over sea ice leads for a microscale, non-eddy-resolving atmosphere model that accounts for the convection over leads of variable width. As a side effect, the derivation of the parametrization and related sensitivity studies helped to better understand the processes involved in the formation and decay of convective plumes in a neutral or slightly stable environment. As a starting point, a previous parametrization by L08 was used, who considered leads of only one particular width (1 km). However, the new and modified parametrization should be more general by including the lead width L as a parameter.

We considered 10 idealized scenarios of a lead-perpendicular flow in a neutrally stratified ABL capped by a strong inversion, and, as in L08, time-averaged LES results were considered for the detailed analysis of the overall lead impact on the ABL. Our LES results revealed that the general characteristics of the flow over leads of different width remained similar to those of the 1 km lead. Namely, a strong plume was developing over the lead and rapidly decaying over the downstream sea ice. This caused an increase of temperature combined with a stabilization downstream of the lead, but with still upward heat fluxes. Thus, the transport was clearly of nonlocal nature. Hence, the basic ideas of L08, applying a nonlocal closure, assuming a separation of turbulence regimes inside and outside the plume region, and assuming decaying turbulence downstream of the lead, remained the same. Thus, also the new parametrization accounts for the inhomogeneous

conditions of convection over leads so that both eddy diffusivity for heat and the nonlocal transport term depend on the distance to the upstream lead edge.

In our parametrization, we assumed fully developed convection above the lead and applied a decay function only over sea ice at the downstream side of a lead. By this assumption, it became possible to consider L as a parameter in the equations. This formulation had a consequence on the parametric equation for the development of the upper IBL height $\delta(y)$, which is equivalent to the top of the convective plume. Two regimes are distinguished in the new formulation, one over the lead and another one downstream of the lead where the decay of turbulence starts. Our assumption is based on the LES results for leads where the convection penetrates into the inversion already above the lead, which we defined as wide leads. Nevertheless, we derived a parametrization where also for narrow leads, where the convection reaches the inversion further downwind, the same set of equations is used. The only difference of our parametrization between wide and narrow leads concerns the development of $\delta(y)$ at $y>L$ since for narrow leads, the limit $\delta(y) \geq z_i$ is not reached at $y < L$. In the limiting case of very narrow leads ($L \rightarrow 0$), the new approach coincides with the $\delta(y)$-formulation of L08.

We showed that results obtained with the new closure agree well with LES, mainly concerning heat flux patterns, plume inclinations, and downstream stratification in the tested range of $z_i = 300$ m, $3 < U < 10$ ms^{-1}, and $85 < F_s < 245$ Wm^{-2}. Unlike L08, we also applied a nonlocal closure for the eddy diffusivity for momentum. With this additional modification, also the horizontal wind speed with a diminishing weak low-level jet over the lead and momentum flux distributions in the convective region were basically reproduced. Furthermore, we showed that also results obtained with our parametrization of higher order moments, such as the vertical velocity variance, agree well with LES. The new parametrization contains six unknown parameters, which were derived using information from LES. We stress that the same set of values for the parameters was used for all cases considered. Nevertheless, there is room for further improvement of the new approach regarding, for example, the representation of entrainment and the height-dependent start of decaying convection downwind of the lead.

Both our LES and microscale model results also point to difficulties that might occur in mesoscale studies of atmospheric processes over the marginal sea ice zone, where leads strongly affect the flow regime. Mostly, such studies apply local closures, and it is obvious that the results of such modeling would have the same drawbacks as our results obtained with a local closure. The largest drawback is that the stabilizing effect of leads on the downstream ABL is completely missing, and the spatial distribution of turbulent fluxes of heat and momentum shows large deviations from the detailed LES results. We expect that the deviations might sum up to large errors when lead ensembles are considered since conditions upstream of a lead in the inner region of such an ensemble might be affected by its upstream neighboring lead. Furthermore, we showed that a nonlocal closure was also necessary for momentum fluxes to obtain a reasonable agreement with LES results.

Altogether, our results obtained with the new parametrization agree well with LES for different L in the wide range of the above-mentioned meteorological forcing. A further development should include explicitly moisture transport as well as variations of the ABL height, wind direction, and upstream stability. Observations of, for example, Tetzlaff et al. (2015) showed that a stable stratification of the upstream ABL influences the IBL-growth. This might affect the parameter a (Equation 20). Nevertheless, the new parametrization represents a clear improvement since now, variable lead widths can be considered for a detailed study of the lead effects on the ABL. We also showed that grid sizes of the microscale model should not exceed $L/5$ to obtain a reasonable agreement of detailed flow structures as with LES. This shows that also for narrow leads in the range of 500 m or 1 km width, horizontal grid sizes of 100 to 200 m are sufficient to reproduce those structures. Thus, compared to LES, numerical costs are much lower for potential sensitivity studies on the lead impact defining also the range of the parameters. Selected studies might then need additional LES for validation. Thus, our findings could help to derive finally an improved surface flux parametrization over the marginal sea ice zone to be used in climate and weather prediction models. Furthermore, the new nonlocal approach might also help to improve parametrizations of a convective IBL developing over inhomogeneous surfaces, in general.

Appendix A: Determination of the Parameters d_w and d_θ

L08 state that their decay length scale D, which determines the strength of the exponential decay of w_l (Equation 9), can be expressed by $D \propto U\tau$, where τ is the large-eddy turnover time with $\tau \approx z_i/w_* \approx z_i^{2/3}/B_l^{1/3}$. We apply this relation to determine the corresponding decay length scale of the new parametrization, D_w, which is used in Equation 19,

$$D_w = d_w \cdot U\frac{z_i^{2/3}}{B_l^{1/3}} = d_w \cdot U\frac{z_i^{2/3}}{\left(\frac{g}{\theta_0}\overline{w'\theta'}|_s\right)^{1/3}} = d_w \cdot U\frac{z_i^{2/3}}{\left(\frac{\frac{g}{\theta_0}\overline{F_s}}{\rho_{0,s}c_p}\right)^{1/3}}, \tag{A1}$$

where $\rho_{0,s} = 1.4\,\mathrm{kgm}^{-3}$ is the air density at the surface. Values of $\overline{F_s}$ are shown in Table 1. Furthermore, we define D_w as the distance (y–L) to the downstream lead edge, where fluctuations of the vertical velocity weakened to the fraction of $1/e$, where e is Euler's number. The vertical velocity fluctuations are, in turn, proportional to the convective velocity scale w_* in horizontally homogeneous conditions in the center of the ABL at $z = 0.4z_i$ (Holtslag & Moeng, 1991). Thus, we consider the square root of the vertical velocity variance, $(\overline{w'^2})^{1/2}$, from LES to determine D_w. Hence, we solve Equation A1 for the proportionality factor d_w and we can determine its value taking all open quantities (D_w, U, z_i, B_l) from LES.

We use all cases with $L \geq 5$ km (Table 1, wide leads) for this determination since we can write $w_l = w_*$ at $y = L$ due to our assumption of horizontally homogeneous conditions if $\delta_L = z_i$ (see section 5.1). With linear regression (Figure A1a), we obtain $d_w \approx 1.7$. Furthermore, we consider Equation A1 with $d_w \approx 1.7$ to determine D_w also for all our simulations with $L < 5$ km since we assume D_w to be independent on L.

Unlike L08, we apply a decay function also for the convective temperature scale θ_l to consider decaying temperature fluctuations $\overline{\theta'^2}$ in the lead's downstream region. Furthermore, we assume differences between decaying temperature and vertical velocity variations; hence, we introduce another decay

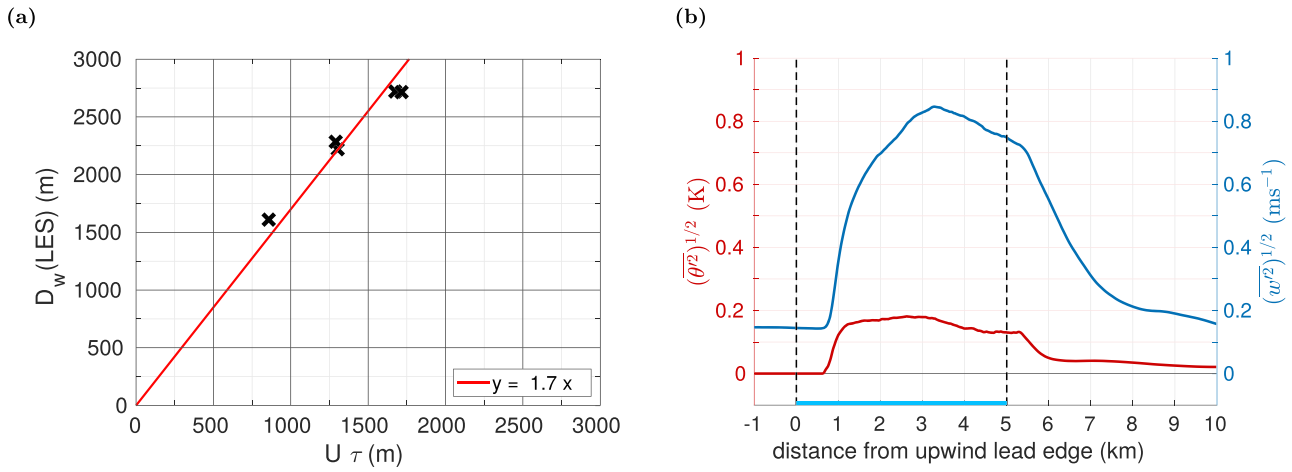

Figure A1. (a) Decay length scale of vertical velocity variations from LES of cases with $L \geq 5$ km (Table 1), D_w, against $U\tau$ (crosses). To determine the parameter d_w, linear regression was performed (red curve with $y = D_w$ and $x = U\tau$). (b) Square roots of the variances of potential temperature in K (red) and vertical velocity in ms^{-1} (blue), $(\overline{\theta'^2})^{1/2}$ and $(\overline{w'^2})^{1/2}$, at $z = 0.4z_i$ along the distance of the upstream lead edge y from the LES of case L5c-U5. The lead is between 0 and 5 km distance.

length scale D_θ. To determine D_θ, we consider the results of Nieuwstadt and Brost (1986), who studied the decay of convective turbulence in the ABL using LES. They proposed that fluctuations in temperature decrease faster than fluctuations in vertical velocity when upward surface heat flux is suddenly stopped. Here, we have a comparable situation, where our results are quasi-stationary on a temporal, but variable on a spatial scale due to suddenly vanishing upward surface heat fluxes at the transition from the lead to the downstream ice. Thus, the convective turbulence decays with increasing distance (y–L) to the downstream lead edge and based on the LES results of Nieuwstadt and Brost (1986), we expect that temperature variations decay after a shorter distance than vertical velocity variations. Namely, Nieuwstadt and Brost (1986) formulated two subgrid time scales for the transfer of momentum and temperature, τ_m and τ_h, and found that $\tau_h \approx 0.3\tau_m$. Therefore, similar to Equation A1, we define

$$D_\theta = d_\theta \cdot U \frac{z_i^{2/3}}{B_l^{1/3}}. \tag{A2}$$

Then, we calculated the square root of the variances of both temperature and vertical velocity, $(\overline{\theta'^2})^{1/2}$ and $(\overline{w'^2})^{1/2}$, at $z = 0.4z_i$ along the distance y from LES of case L5c-U5 (Figure A1b). Indeed, from this Figure we find that temperature fluctuations already decrease at y–$L \approx 1$ km to a constant level, whereas vertical velocity fluctuations reach a constant level at y–$L \approx 3$ km. Thus we confirm the finding

$$d_\theta \approx 0.3\, d_w \tag{A3}$$

of Nieuwstadt and Brost (1986) with our LES results and use this in the new parametrization.

Appendix B: Determination of the Parameters *c* and *a*

Also c and a (values see section 5.1) were obtained using our LES results. The parameter c acts as an adjustable constant for the convective velocity scale $w_l(y)$ (Equation 19) in the new parametrization. When we assume the validity of Equation 26, which goes back to Holtslag and Moeng (1991), we can obtain an equation for c. The first step is to use the definitions (14) and (15) in Equation 26 for S and Z and replace w_l then by Equation 19. We need to consider only the upper line of Equation 19 because we aim to validate the assumption $c = 1$ for the region over the lead where $\delta(y) = z_i$. The next step is to solve this equation for c, which results in

$$c(y,z) = \left(\frac{\overline{w'^2(y,z)}^{3/2} - 1.6^{3/2} u_*(y)^3 \left(1 - \frac{z}{\delta(y)}\right)^{3/2}}{1.2 B_l(y) z \left(1 - 0.9\frac{z}{\delta(y)}\right)^{3/2}} \right)^{1/3}, \; 0 \le y \le L, \tag{B1}$$

where $u_*(y)$, $\overline{w'^2(y,z)}$, and $B_l(y)$ are calculated from LES. To obtain $\delta(y)$ from LES results, we used for each considered case a linear approximation of the upper plume boundary in the region $0 \le y \le y_{z_i}$, where y_{z_i} denotes the intersection of δ with z_i. For $y > y_{z_i}$, the value of δ was set to z_i. The linear fit was derived from Figures S4 and S5 showing the heat flux obtained with LES since there the upper plume boundary $\delta(y)$ is clearly visible. The distribution of $c(y,z)$ as obtained finally from Equation B1 with the help of LES is shown in Figure B1 for all cases with $L \ge 5$ km.

It is shown that $c(y,z)$ as obtained from Equation B1 varies in both horizontal and vertical direction, especially in the region for which $\delta(y) < z_i$. However, in the region with $\delta(y) = z_i$, the value $c(y,z) = 1$

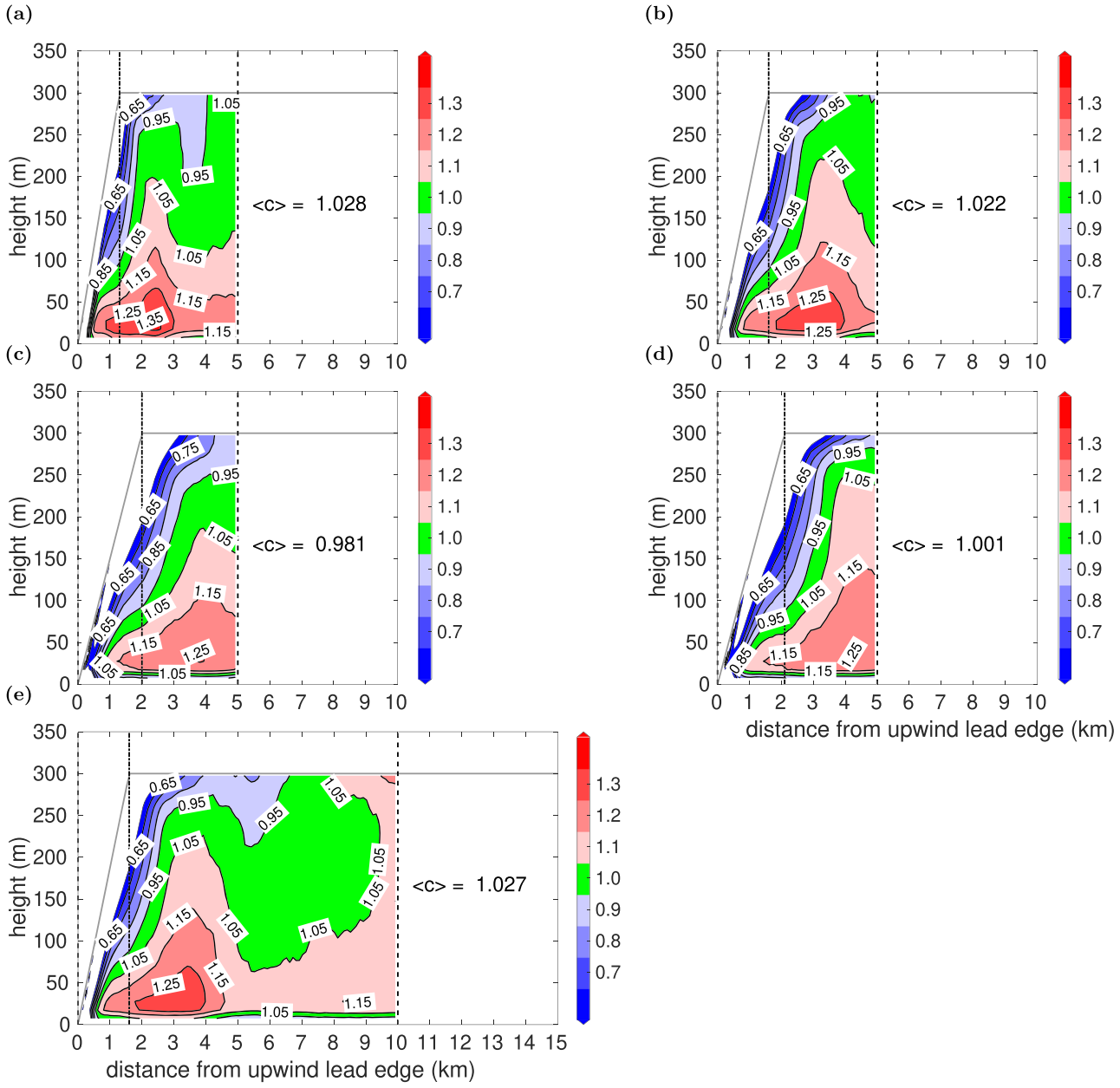

Figure B1. Distribution of $c(y,z)$ via Equation B1 from LES for all cases with $L \geq 5$ km and mean values $\langle c \rangle$ for the region where $y_{z_i} \leq y < L$ (between the dashed-dotted and dashed lines) and where $0 < z < z_i$. Cases are L5c-U3 (a), L5c-U5 (b), L5c-U7 (c), L5w-U5 (d), and L10c-U5 (e). The solid gray lines are linear approximations of the IBL height $\delta(y)$ obtained from LES (Figures S4 and S5). The position of the lead is between 0 km and the vertical dashed black line.

dominates. This holds especially for the cases L5c-U3 and L10c-U5 where horizontally homogeneous conditions over the lead are most pronounced (see Figures 2a and 2g). Furthermore, averaged over the respective regions where $\delta(y) = z_i$, we obtain $\langle c(y, z) \rangle \approx 1$ (Figure B1). Despite the deviations of c from 1 in some regions, we found that this value could be used in all our cases as a rough approximation, also where $\delta(y) < z_i$ and also in the lead's downstream region. Note also that with our assumptions w_l depends only on y but not on z, while $\overline{w'^2}$ depends on both y and z.

Table B1
Values Derived Based on Figures S4 and S5 for all Cases to Obtain the Parameter a in the new Parametrization

Wide leads	L5c-U3	L5c-U5	L5c-U7	L10c-U5	L5w-U5
y_{z_i} (m)	1300	1600	2000	1600	2100
a	0.99	1.21	1.25	1.22	1.21
Narrow leads	**L1c-U3**	**L1c-U5**	**L1c-U7**	**L1w-U10**	**L0.5c-U5**
y_{z_i} (m)	1180	1570	1950	3720	1650
a	1.14	1.34	1.45	1.45	1.45

Note. For each case (see Table 1), y_{z_i} is approximately the position (m) where the plume intersects with the inversion at $z_i = 300$ m as simulated with LES (see Figures S4 and S5). Values for a are obtained via Equation B2

The parameter a determines the plume inclination. After transforming Equation 20, we obtain:

$$a(y) = \begin{cases} \left(\dfrac{\delta(y)}{\left(\dfrac{2B_l^{1/3}}{3\ U} y \right)^{3/2}} \right)^{2/3}, & 0 \le y \le L \\ \left(\dfrac{\delta(y)}{\left(\dfrac{2B_l^{1/3}}{3\ U} L \right)^{3/2} \left(1 + \dfrac{D_w}{L} \left(1 - \exp\left(\dfrac{L-y}{D_w} \right) \right) \right)^{3/2}} \right)^{2/3}, & y > L \end{cases} \quad \text{(B2)}$$

To determine a, we use both B_l and U from LES and assume again a linear increase of $\delta(y)$ with y (see Figures S4 and S5). Thus, we can insert any arbitrary pair of $\delta(y)$ and y resulting from the linear line $\delta(y)$ obtained from LES in the above equation. This leads finally to the values for a shown in Table B1 for all cases. Obviously, they range from 0.98 to 1.45. Table B1 also shows that a depends on B_l, U, and L. However, for simplicity, we prescribe the value $a = 1.2$ for all cases (see also section 5.4).

Appendix C: Sensitivity of Microscale Model Results on the Horizontal Resolution

For case L5c-U5, we repeated the METRAS simulations using the new parametrization for horizontal grid sizes of Δy = 100, 500, 1,000, and 2,500 m (Figures C1 and C2). Both figures show that the overall structure of the patterns depends only marginally on Δy up to $\Delta y = 1{,}000$ m, which is equal to $L/5$ in this case. With $\Delta y =$ 2,500 m and, thus, only two grid points to resolve the lead, some structures change significantly (Figures C1g and C1h and C2g and C2h). Thus, to reproduce detailed flow structures over the lead, grid sizes of not more than $L/5$ seem necessary to obtain a reasonable agreement with LES.

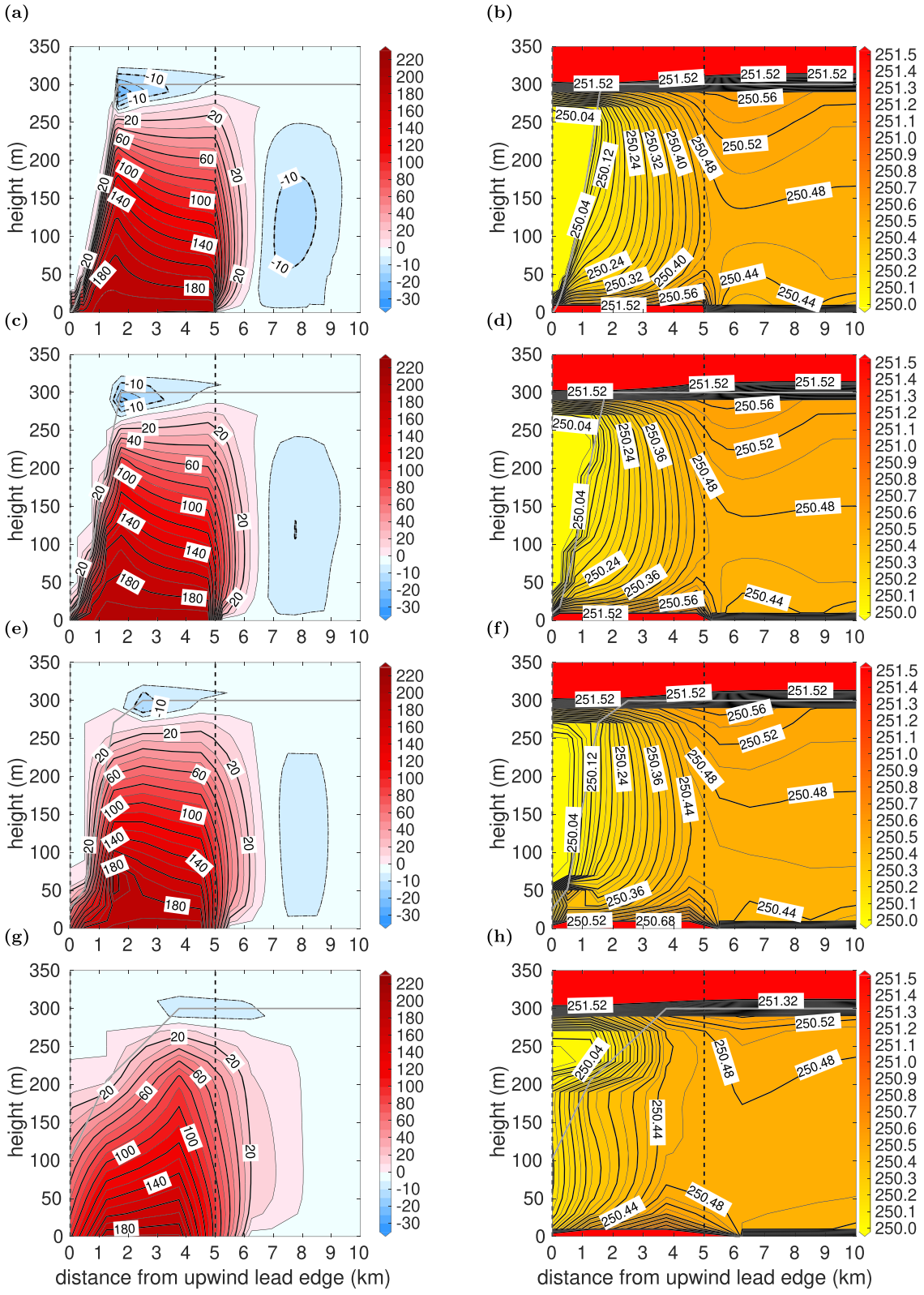

Figure C1. METRAS results of heat flux in Wm^{-2} (left column) as in Figure 7c and potential temperature in K (right column), but obtained with other horizontal grid sizes. $\Delta y = 100$ m (a, b), $\Delta y = 500$ m (c, d), $\Delta y = 1{,}000$ m (e, f), and $\Delta y = 2{,}500$ m (g, h). For the corresponding LES results, see Figure 2c.

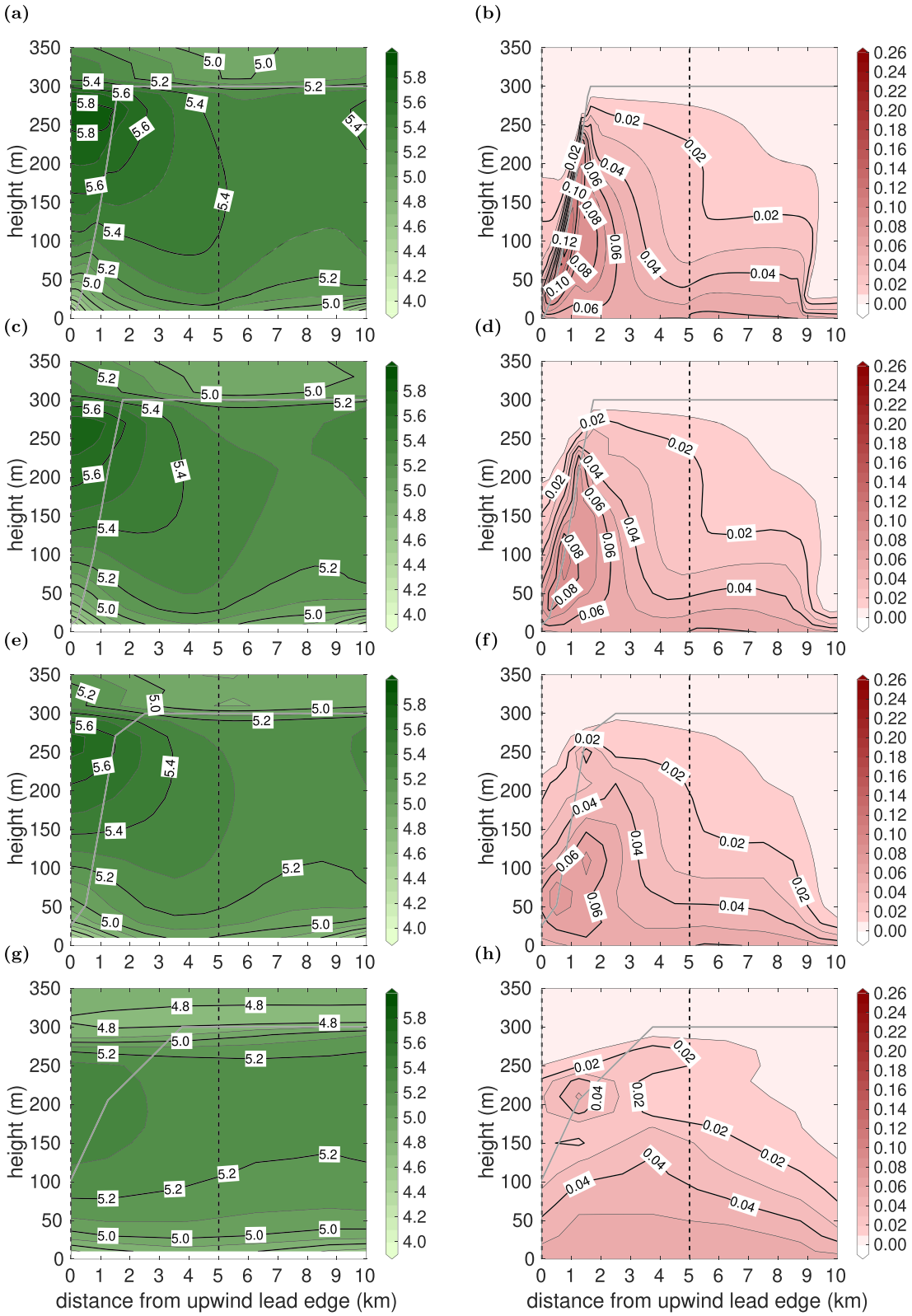

Figure C2. METRAS results of horizontal wind speed in ms^{-1} (left column) and vertical momentum flux in Nm^{-2} (right column) as in Figures 8c and 8d, but obtained with different horizontal grid sizes. $\Delta y = 100$ m (a, b), $\Delta y = 500$ m (c, d), $\Delta y = 1{,}000$ m (e, f), and $\Delta y = 2{,}500$ m (g, h). For the corresponding LES results, see Figures 3c and 3d.

Data Availability Statement

The LES data are available on PANGAEA repository (Zhou & Gryschka, 2019). An authorized version of the METRAS code is available on request at University Hamburg, see technical report (Schlünzen et al., 2012).

Acknowledgments

We thank Tim Gollnik for providing subroutines in METRAS for the flux calculation and for further support to run the model at the German Climate Computing Center (DKRZ). The PALM simulations were performed with resources provided by the North-German Supercomputing Alliance (HLRN). Processing of all data and their visualization were done with MatLab 2019a and 2019b. The study was supported by DFG (grant LU 818/5-1 and GR 4911/1-1). We gratefully acknowledge also the funding by the Deutsche Forschungsgemeinschaft (DFG, German Research Foundation) Project number 268020496 TRR 172 within the Transregional Collaborative Research Center ArctiC Amplification: Climate Relevant Atmospheric and SurfaCe Processes, and Feedback Mechanisms (AC)3. We also thank two anonymous reviewers for constructive criticism, which helped to improve the quality of this manuscript. Also comments of Cedrick Ansorge were helpful for improvements.

References

Alam, A., & Curry, J. A. (1995). Lead-induced atmospheric circulations. *Journal of Geophysical Research*, *100*(C3), 4643–4651. https://doi.org/10.1029/94JC02562

Alam, A., & Curry, J. A. (1997). Determination of surface turbulent fluxes over leads in Arctic sea ice. *Journal of Geophysical Research*, *102*(C2), 3331–3343. https://doi.org/10.1029/96JC03606

Andreas, E. L., & Cash, B. A. (1999). Convective heat transfer over wintertime leads and polynyas. *Journal of Geophysical Research*, *104*(C11), 25,721–25,734. https://doi.org/10.1029/1999JC900241

Andreas, E. L., Paulson, C. A., William, R. M., Lindsay, R. W., & Businger, J. A. (1979). The turbulent heat flux from Arctic leads. *Boundary-Layer Meteorology*, *17*(1), 57–91. https://doi.org/10.1007/BF00121937

Badgley, F. I. (1966). Heat balance at the surface of the Arctic Ocean. In *Proceedings of the Symposium on the Arctic Heat Budget and Atmospheric Circulation* (J. O. Fletcher, Ed.), Rand Corporation (RM-5233-NSF), Santa Monica, CA, pp. 215–246.

Batrak, Y., & Müller, M. (2018). Atmospheric response to kilometer-scale changes in sea ice concentration within the marginal ice zone. *Geophysical Research Letters*, *45*, 6702–6709. https://doi.org/10.1029/2018GL078295

Blackadar, A. K. (1962). The vertical distribution of wind and turbulent exchange in a neutral atmosphere. *Journal of Geophysical Research*, *67*(8), 3095–3102. https://doi.org/10.1029/JZ067i008p03095

Brown, A. R. (1996). Evaluation of parametrization schemes for the convective boundary layer using large-eddy simulation results. *Boundary-layer Meteorology*, *81*(2), 167–200. https://doi.org/10.1007/BF00119064

Businger, J. A., Wyngaard, J. C., Izumi, Y., & Bradley, E. F. (1971). Flux-profile relationships in the atmospheric surface layer. *Journal of the Atmospheric Sciences*, *28*(2), 181–189. https://doi.org/10.1175/1520-0469(1971)028 < 0181:FPRITA>2.0.CO;2

Chechin, D. G., Makhotina, I. A., Lüpkes, C., & Makshtas, A. P. (2019). Effect of wind speed and leads on clear-sky cooling over Arctic sea ice during polar night. *Journal of the Atmospheric Sciences*, *76*(8), 2481–2503. https://doi.org/10.1175/JAS-D-18-0277.1

Dare, R. A., & Atkinson, B. W. (2000). Atmospheric response to spatial variations in concentration and size of polynyas in the Southern Ocean sea-ice zone. *Boundary-Layer Meteorology*, *94*(1), 65–88. https://doi.org/10.1023/A:1002442212593

de Roode, S. R., Frederikse, T., Siebesma, A. P., Ackerman, A. S., Chylik, J., Field, P. R., et al. (2019). Turbulent transport in the gray zone: A large eddy model intercomparison study of the CONSTRAIN cold air outbreak case. *Journal of Advances in Modeling Earth Systems*, *11*, 597–623. https://doi.org/10.1029/2018MS001443

Deardorff, J. W. (1970). Convective velocity and temperature scales for the unstable planetary boundary layer and for Rayleigh convection. *Journal of the Atmospheric Sciences*, *27*(8), 1211–1213. https://doi.org/10.1175/1520-0469(1970)027 < 1211:CVATSF>2.0.CO;2

Deardorff, J. W. (1972). Theoretical expression for the countergradient vertical heat flux. *Journal of Geophysical Research*, *77*(30), 5900–5904. https://doi.org/10.1029/JC077i030p05900

Deardorff, J. W., & Peterson, E. W. (1980). The boundary-layer growth equation with Reynolds averaging. *Journal of the Atmospheric Sciences*, *37*(6), 1405–1409. https://doi.org/10.1175/1520-0469(1980)037 < 1405:TBLGEW>2.0.CO;2

Dyer, A. J. (1974). A review of flux-profile relationships. *Boundary-Layer Meteorology*, *7*(3), 363–372. https://doi.org/10.1007/BF00240838

Esau, I. N. (2007). Amplification of turbulent exchange over wide Arctic leads: Large-eddy simulation study. *Journal of Geophysical Research*, *112*, D08109. https://doi.org/10.1029/2006JD007225

Glendening, J. W. (1994). Dependence of a plume heat budget upon lateral advection. *Journal of the Atmospheric Sciences*, *51*(23), 3517–3530. https://doi.org/10.1175/1520-0469(1994)051 < 3517:DOAPHB>2.0.CO;2

Glendening, J. W., & Burk, S. D. (1992). Turbulent transport from an Arctic lead: A large-eddy simulation. *Boundary-Layer Meteorology*, *59*(4), 315–339. https://doi.org/10.1007/BF02215457

Gollnik, T. (2008). Parametrisierung turbulenter Flüsse über Eisrinnen mit einem mikroskaligen Atmosphärenmodell (Diploma thesis), Germany.

Grachev, A. A., Andreas, E. L., Fairall, C. W., Guest, P. S., & Persson, P. O. G. (2013). The critical Richardson number and limits of applicability of local similarity theory in the stable boundary layer. *Boundary-Layer Meteorology*, *147*(1), 51–82. https://doi.org/10.1007/s10546-012-9771-0

Gryschka, M., Drüe, C., Etling, D., & Raasch, S. (2008). On the influence of sea-ice inhomogeneities onto roll convection in cold-air outbreaks. *Geophysical Research Letters*, *35*, L23804. https://doi.org/10.1029/2008GL035845

Gryschka, M., Fricke, J., & Raasch, S. (2014). On the impact of forced roll convection on vertical turbulent transport in cold air outbreaks. *Journal of Geophysical Research: Atmospheres*, *119*, 12,513–12,532. https://doi.org/10.1002/2014JD022160

Hartmann, J., Albers, F., Argentini, S., Borchert, A., Bonafé, U., Cohrs, W., et al. (1999). Arctic Radiation and Turbulence Interaction Study (ARTIST). Reports on Polar Research 305, https://doi.org/10.2312/BzP_0305_1999

Hartmann, J., Kottmeier, C., & Wamser, C. (1992). Radiation and Eddy Flux Experiment 1991 (REFLEX I). Reports on Polar Research 105, https://doi.org/10.2312/BzP_0105_1992

Herbert, F., & Kramm, G. (1985). Trockene Deposition reaktionsträger Substanzen, beschrieben mit einem diagnostischen Modell der bodennahen Luftschicht. In K. H. Becker, & J. Löbel (Eds.), *Atmosphärische Spurenstoffe und ihr physikalisch-chemisches Verhalten* (pp. 190–209). Heidelberg, Germany: Springer, Berlin.

Holtslag, A. A. M., & Moeng, C.-H. (1991). Eddy diffusivity and countergradient transport in the convective atmospheric boundary layer. *Journal of the Atmospheric Sciences*, *48*(14), 1690–1698. https://doi.org/10.1175/1520-0469(1991)048 < 1690:EDACTI>2.0.CO;2

Kataoka, H., & Mizuno, M. (2002). Numerical flow computation around aeroelastic 3 d square cylinder using inflow turbulence. *Wind and Structures*, *5*(2/4), 379–392. https://doi.org/10.12989/was.2002.5.2_3_4.379

Kottmeier, C., Hartmann, J., Wamser, C., Bochert, A., Lüpkes, C., Freese, D., & Cohrs, W. (1994). Radiation and Eddy Flux Experiment 1993 (REFLEX II). Reports on Polar Research 133. https://doi.org/10.2312/BzP_0133_1994

Lüpkes, C., Gryanik, V. M., Witha, B., Gryschka, M., Raasch, S., & Gollnik, T. (2008). Modeling convection over arctic leads with LES and a non-eddy-resolving microscale model. *Journal of Geophysical Research*, *113*, C09028. https://doi.org/10.1029/2007JC004099

Lüpkes, C., Hartmann, J., Birnbaum, G., Cohrs, W., Yelland, M., Pascal, R., et al. (2004). Convection over Arctic leads (COAL). In U. Schauer, & G. Kattner (Eds.), *The expedition ARKTIS XIX/1 a, b and XIX/2 of the research vessel POLARSTERN in 2003* (Vol. 481, pp. 47–62). Bremerhaven, Germany: Alfred Wegener Institute for Polar and Marine Research.

Lüpkes, C., & Schlünzen, K. H. (1996). Modelling the Arctic convective boundary-layer with different turbulence parameterizations. *Boundary-Layer Meteorology*, *79*(1-2), 107–130. https://doi.org/10.1007/BF00120077

Lüpkes, C., Vihma, T., Birnbaum, G., & Wacker, U. (2008). Influence of leads in sea ice on the temperature of the atmospheric boundary layer during polar night. *Geophysical Research Letters*, *35*, L03805. https://doi.org/10.1029/2007GL032461

Li, X., Krueger, S. K., Strong, C., Mace, G. G., & Benson, S. (2020). Midwinter arctic leads form and dissipate low clouds. *Nature Communications*, *11*(1), 1–8. https://doi.org/10.1038/s41467-019-14074-5

Lindsay, R. W., & Rothrock, D. A. (1995). Arctic sea ice leads from advanced very high resolution radiometer images. *Journal of Geophysical Research*, *100*(C3), 4533–4544. https://doi.org/10.1029/94JC02393

Lund, T. S., Wu, X., & Squires, K. D. (1998). Generation of turbulent inflow data for spatially-developing boundary layer simulations. *Journal of Computational Physics*, *140*(2), 233–258. https://doi.org/10.1006/jcph.1998.5882

Müller, M., Batrak, Y., Kristiansen, J., Køltzow, M. A., Noer, G., & Korosov, A. (2017). Characteristics of a convective-scale weather forecasting system for the european arctic. *Monthly Weather Review*, *145*(12), 4771–4787. https://doi.org/10.1175/MWR-D-17-0194.1

Makshtas, A. P., & Nikolaev, I. V. (1991). *The heat budget of Arctic ice in the winter*. Cambridge: International Glaciological Society.

Marcq, S., & Weiss, J. (2012). Influence of sea ice lead-width distribution on turbulent heat transfer between the ocean and the atmosphere. *The Cryosphere*, *6*, 143–156. https://doi.org/10.5194/tc-6-143-2012

Maronga, B., Gryschka, M., Heinze, R., Hoffmann, F., Kanani-Sühring, F., Keck, M., et al. (2015). The Parallelized Large-Eddy Simulation Model (PALM) version 4.0 for atmospheric and oceanic flows: model formulation, recent developments, and future perspectives. *Geoscientific Model Development Discussions*, *8*(2), 1539–1637. https://doi.org/10.15488/27

Mauritsen, T., Svensson, G., & Grisogono, B. (2005). Wave flow simulations over Arctic leads. *Boundary-Layer Meteorology*, *117*(2), 259–273. https://doi.org/10.1007/s10546-004-1427-2

Maykut, G. A. (1978). Energy exchange over young sea ice in the central Arctic. *Journal of Geophysical Research*, *83*(C7), 3646–3658. https://doi.org/10.1029/JC083iC07p03646

Miles, M. W., & Barry, R. G. (1998). A 5-year satellite climatology of winter sea ice leads in the western Arctic. *Journal of Geophysical Research*, *103*(C10), 21,723–21,734. https://doi.org/10.1029/98JC01997

Monin, A. S., & Yaglom, A. M. (1971). *Statistical fluid dynamics Vol. 1*. Cambridge: MIT Press, Cambridge Mass.

Nieuwstadt, F. T. M., & Brost, R. A. (1986). The decay of convective turbulence. *Journal of the Atmospheric Sciences*, *43*(6), 532–546. https://doi.org/10.1175/1520-0469(1986)043 < 0532:TDOCT>2.0.CO;2

Noh, Y., Cheon, W. G., Hong, S. Y., & Raasch, S. (2003). Improvement of the K-profile model for the planetary boundary layer based on large eddy simulation data. *Boundary-layer Meteorology*, *107*(2), 401–427. https://doi.org/10.1023/A:1022146015946

Orlanski, I. (1976). A simple boundary condition for unbounded hyperbolic flows. *Journal of Computational Physics*, *21*(3), 251–269. https://doi.org/10.1016/0021-9991(76)90023-1

Overland, J. E., McNutt, S. L., Groves, J., Salo, S., Andreas, E. L., & Persson, P. O. G. (2000). Regional sensible and radiative heat flux estimates for the winter Arctic during the Surface Heat Budget of the Arctic Ocean (SHEBA) experiment. *Journal of Geophysical Research*, *105*(C6), 14,093–14,102. https://doi.org/10.1029/1999JC000010

Paulson, C. A., & Smith, J. D. (1974). The AIDJEX lead experiment. In A. Johnson (Ed.), *AIDJEX Bulletin No. 23* (pp. 1–8). Seattle, Washington: University of Washington.

Pinto, J. O., Alam, A., Maslanik, J. A., Curry, J. A., & Stone, R. S. (2003). Surface characteristics and atmospheric footprint of springtime Arctic leads at SHEBA. *Journal of Geophysical Research*, *108*(C4), 8051. https://doi.org/10.1029/2000JC000473

Priestley, C. H. B., & Swinbank, W. C. (1947). Vertical transport of heat by turbulence in the atmosphere. *Proceedings of the Royal Society of London. Series A. Mathematical and Physical Sciences*, *189*(1019), 543–561. https://doi.org/10.1098/rspa.1947.0057

Raasch, S., & Schröter, M. (2001). PALM - A large-eddy simulation model performing on massively parallel computers. *Meteorologische Zeitschrift*, *10*(5), 363–372. https://doi.org/10.1127/0941-2948/2001/0010-0363

Schlünzen, K. H., Bungert, U., Flagg, D. D., Fock, B. H., Gierisch, A., Grawe, D., et al. (2012). Technical Documentation of the Multiscale Model System M-SYS (METRAS, MITRAS, MECTM, MICTM, MESIM) (*3*): Meteorologisches Institut, Universität Hamburg. https://www.mi.uni-hamburg.de/en/arbeitsgruppen/memi/modelle/dokumentation/msys-technical-documentation.pdf

Schlünzen, K. H., Flagg, D. D., Fock, B. H., Gierisch, A., Lüpkes, C., Reinhardt, V., & Spensberger, C. (2012). Scientific Documentation of the Multiscale Model System M-SYS (METRAS, MITRAS, MECTM, MICTM, MESIM) (*4*): Meteorologisches Institut, Universität Hamburg. https://www.mi.uni-hamburg.de/en/arbeitsgruppen/memi/modelle/dokumentation/msys-scientific-documentation.pdf

Siebesma, A. P., Soares, P. M. M., & Teixeira, J. (2007). A combined eddy-diffusivity mass-flux approach for the convective boundary layer. *Journal of the Atmospheric Sciences*, *64*(4), 1230–1248. https://doi.org/10.1175/JAS3888.1

Smith, S. D., Anderson, R. J., Hartog, G. D., Topham, D. R., & Perkin, R. G. (1983). An investigation of a polynya in the Canadian Archipelago: 2. Structure of turbulence and sensible heat flux. *Journal of Geophysical Research*, *88*(C5), 2900–2910. https://doi.org/10.1029/JC088iC05p02900

Smith, S. D., Muench, R. D., & Pease, C. H. (1990). Polynyas and leads: An overview of physical processes and environment. *Journal of Geophysical Research*, *95*(C6), 9461–9479. https://doi.org/10.1029/JC095iC06p09461

Stull, R. B. (1988). *An introduction to boundary layer meteorology*. Dordrecht, The Netherlands: Kluwer Academic Publishers.

Tetzlaff, A. (2016). Convective processes in the polar atmospheric boundary layer: a study based on measurements and modeling (Doctoral dissertation), Universität Bremen: Physik/Elektrotechnik.

Tetzlaff, A., Lüpkes, C., & Hartmann, J. (2015). Aircraft-based observations of atmospheric boundary-layer modification over Arctic leads. *Quarterly Journal of the Royal Meteorological Society*, *141*(692), 2839–2856. https://doi.org/10.1002/qj.2568

Thorndike, A. S., Rothrock, D. A., Maykut, G. A., & Colony, R. (1975). The thickness distribution of sea ice. *Journal of Geophysical Research*, *80*(33), 4501–4513. https://doi.org/10.1029/JC080i033p04501

Turner, J. S. (1986). Turbulent entrainment: the development of the entrainment assumption, and its application to geophysical flows. *Journal of Fluid Mechanics*, *173*, 431–471. https://doi.org/10.1017/S0022112086001222

Vihma, T., Pirazzini, R., Fer, I., Renfrew, I. A., Sedlar, J., Tjernström, M., et al. (2014). Advances in understanding and parameterization of small-scale physical processes in the marine Arctic climate system: a review. *Atmospheric Chemistry and Physics (ACP)*, *14*(17), 9403–9450. https://doi.org/10.5194/acpd-13-32703-2013

Weinbrecht, S., & Raasch, S. (2001). High-resolution simulations of the turbulent flow in the vicinity of an Arctic lead. *Journal of Geophysical Research*, *106*(C11), 27,035–27,046. https://doi.org/10.1029/2000JC000781

Wenta, M., & Herman, A. (2018). The influence of the spatial distribution of leads and ice floes on the atmospheric boundary layer over fragmented sea ice. *Annals of Glaciology*, *59*(76pt2), 213–230. https://doi.org/10.1017/aog.2018.15

Zhou, X., & Gryschka, M. (2019). Convection over sea ice leads: Large eddy simulation data. PANGAEA. https://doi.pangaea.de/10.1594/PANGAEA.908520

Zulauf, M. A., & Krueger, S. K. (2003). Two-dimensional numerical simulations of Arctic leads: Plume penetration height. *Journal of Geophysical Research*, *108*(C2), 8050. https://doi.org/10.1029/2000JC000495